5

Understanding the Phase Behavior, Rheology and Processing of Carbon Nanotube Suspensions

Anson W. K. Ma[*], Sahil R. Vora

Department of Chemical and Biomolecular Engineering, and Polymer Program, Institute of Materials Science, University of Connecticut, Storrs, Connecticut 06269, United States
[*]Corresponding author

Outline

Introduction

Carbon nanotubes (CNTs) belong to a relatively novel class of nano-scale fibers[1,2] and are one of the most studied materials of the last two decades. They can be classified as either single-wall (SWNTs) or multi-wall (MWNTs), depending on the number of graphene layers that form the tube. Given their low density, high mechanical strength[1,2] and exceptional conductivity,[3,4] they offer great promise for a number of potential applications,[5-9]such as composites and nano-electronics. CNTs have also been coined as the “ultimate polymer”.[10,11] Contemporary advances in synthetic methods[12-16] are now allowing for CNT production in gram and, increasingly, kilogram-scale quantities, enabling systematic and detailed scientific study. For applications that seek to exploit the electronic properties of SWNTs, a key challenge is to control their chirality. This constitutes an active area of research, and could potentially be achieved either during the growth process[17-22] or through purification and separation after growth[23-26]. Irrespective of their electronic properties, a key challenge, from the perspective of materials processing, is the ability to manipulate CNTs at the nano-scale and efficiently process them into macroscopic articles[8], such as fibers or films, in a scalable and commercially viable way. Of particular interest is how CNTs behave in and modify a medium in which they have been suspended, which is the emphasis of this chapter.

Over the last decade, the flow behavior, or rheology, of CNTs has been studied extensively for a wide range of host fluids[27-42] and a physical picture is slowly emerging. However, caution should also be taken in analyzing and directly comparing such results, as CNTs used in different studies can vary significantly in terms of purity, length, diameter, polydispersity (diameter and length), or number of graphene layers. A further complication is that interactions between CNTs can be modified by means of functionalization[43-46] or through the use of a suitable solvent.[47,48] Functionalization can be covalent[46] or non-covalent[45] in nature. There is a huge variation in the type of chemicals used and the effectiveness of such functionalization schemes, but the common idea is to introduce chemical functional groups or surfactant molecules to disrupt and reduce the intrinsic van der Waals attraction between the CNTs, thereby suppressing their natural tendency to aggregate and rendering them soluble in ordinary solvents.

This chapter focuses on systems where CNTs are added to a Newtonian suspending medium, a scenario of relevance to practical applications where CNTs are used either in pure form[49, 50] or as an additive[51,52]. Additionally, understanding the rheological behavior of such fluids helps advance the fundamental understanding of CNT systems, as the intrinsic behavior of the CNTs is less likely to be masked by the rheology of the suspending medium. This chapter is structured in the following way: we first review the physics of individual CNTs suspended in a fluid before considering their collective effect on the suspension as a whole. When dispersed in a solvent, CNTs can form either disordered isotropic phases or liquid-crystalline phases with high degree of local orientational ordering. The morphology of CNT suspensions depends largely on the choice of solvent, dispersion technique and concentration levels. The second part of this chapter highlights some of these CNT systems and their characteristic rheology. This is then followed by a brief review of the various experimental techniques used to characterize the micro/nanostructure of CNT suspensions. Some general observations on the flow microstructure of CNT suspensions are summarized, offering insights into the underlying physics and rheology. We then discuss two quantitative models that have been inspired by these observations. These models are successful in capturing the experimental steady shear rheology of aggregating and non-aggregating CNT suspensions. Finally, some key research questions that remain to be answered are discussed at the end of the chapter.

Bending dynamics of individual Single-Walled CNTs (SWNTs)

Before discussing the behavior of CNTs as a collection of rods in suspensions, it is useful to review the current understanding of CNTs as individual entities. In the literature, there are different views on whether CNTs are rigid or semi-flexible rods. In this regard, the work of Fakhri et al.[53] provide important insight into the behavior of (non-interacting) CNTs suspended in a viscous fluid at extremely low concentration (1-10 ng/mL). By exploiting the intrinsic bandgap fluorescence of semi-conducting SWNTs in the near infrared, Fakhri and co-workers successfully imaged individual SWNTs in the absence of an external field and captured the bending dynamics due to thermal fluctuations (Fig. 5.1).

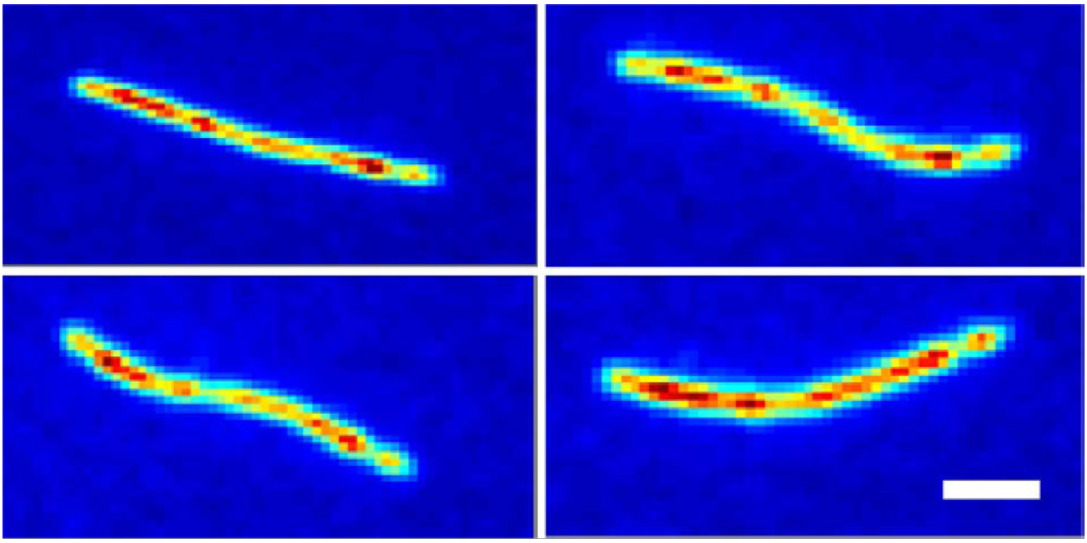

FIGURE 5.1
A series of fluorescence images showing the bending dynamics of a SWNT as it is suspended in 1% (wt) of sodium dodecylbenzenesulfonate (SDBS) aqueous solution. Scale bar = 2 µm. Reproduced from [53]

The persistence length was then calculated from the thermal shape fluctuations for SWNTs with a diameter that varied from 0.7 to 1.2 nm. Their results showed that the persistence length (L_p) varied from 26 to 138 µm and scaled with the cubic power of the diameter, consistent with the prediction of an elastic continuum model. The persistence length identified is much larger than ordinary polymer molecules; for example, the persistence length of poly-paraphenylene terephthalamide (PPTA) is 30 nm and that of poly-p-phenylenebenzobisoxazole (PBO) is 60 – 120 nm.[10] The experimental bending stiffness is about two times higher than that obtained from *ab initio* calculations. The reason for such a discrepancy still remains unclear, but the authors claimed that there was negligible stiffening effect from the ionic surfactant that was used to disperse the SWNTs. As the bending dynamics is strongly affected by the environment in which the SWNTs are suspended, the authors proposed using SWNTs of varied and known persistence length as nanoscale probes for measuring the micro-rheological properties of complex fluids and soft matter.

General flow characteristics in dilute and semi-dilute regimes

It is common to classify rod suspensions according to concentration. Four regimes can be classified; namely, dilute, semi-dilute, and isotropic concentrated and nematic, as illustrated in Fig. 5.2 [54]. In the "dilute" regime, rods can rotate freely without being impeded by other rods, whereas in "semi-dilute" suspensions the rotary motion is impeded but one can still add a new rod randomly into the system with negligible probability of intersecting any other existing rods. The transition between dilute and semi-dilute concentration regimes, $\phi_{d\to s}$, can be defined by considering the ratio of the volume of one rod to the volume of a sphere that the rod can sweep out by rotation about its center of mass[54]:

$$\phi_{d\to s} = \frac{\pi r^2 L}{\frac{1}{6}\pi L^3} = 6\left(\frac{r}{L}\right)^2 \tag{1}$$

where *r* is the radius of the rod and *L* is the length. Eqn (1) gives an estimate of the concentration (by volume) where the transition should occur. However, the experimental transition usually occurs at much higher concentration, typically 5 times larger than that predicted by eqn (1), as a probable result of the rods "dodging" each other.[55] The transition from semi-dilute to concentrated regimes is given in Eqn (2).[54, 55] However, Eqn (2) assumes the rods or CNTs of interest are perfectly rigid, which may not be the case as explained in the previous section.

$$\phi_{s\to c} = \frac{\pi r}{2L} \tag{2}$$

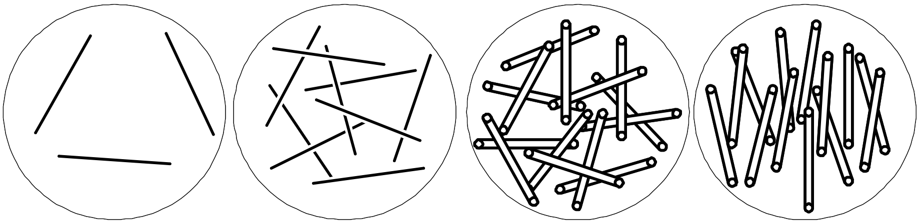

FIGURE 5.2
Four concentration regimes of rod suspensions: (a) dilute, (b) semidilute, (c) isotropic concentrated, and (d) liquid crystalline. Reproduced from [54]

In this section, we will focus mainly on typical flow characteristics of CNT suspensions in the dilute and semi-dilute concentration regimes.

Steady shear flow

As semi-dilute CNT suspensions are subjected to steady shear flow, they generally show a shear-thinning characteristic where the suspension viscosity decreases as shear rate increases[27, 28, 56, 57].

This type of behavior is not unique to CNT suspensions and is shared by other systems,[58] including flexible and semi-flexible polymer solutions. Nevertheless, it is worth noting that incorporation of a relatively small amount of CNT can drastically increase the viscosity of a suspending medium, this being especially true in the case of CNT suspensions showing aggregate structures.[28, 57] Figure 5.3 shows the suspension viscosity as a function of shear rate as different concentrations of CNT suspensions are subjected to steady shear flow[59].

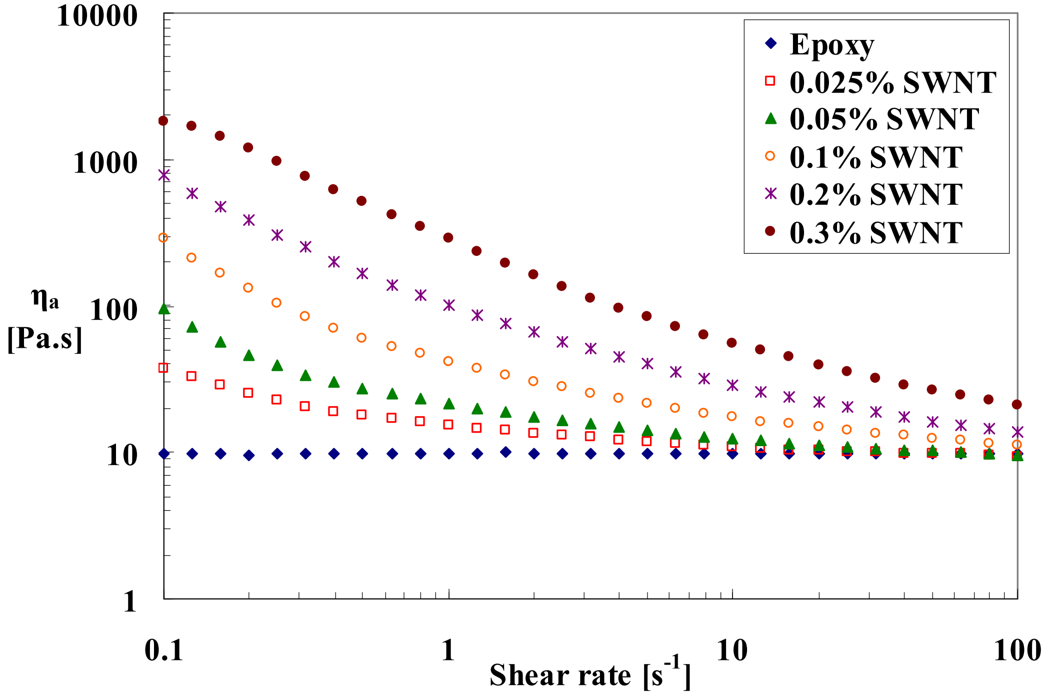

FIGURE 5.3
Apparent steady shear viscosity (η_a) versus shear rate for epoxy and five different concentrations (wt%) of (as-produced) SWNTs suspended in epoxy (without hardener). The SWNTs were produced by the high-pressure carbon monoxide (HiPco) method[16]. Temperature = 25°C. Reproduced from [59]

As shown in the figure, addition of 0.1% (wt) of (as-produced) SWNTs increases the viscosity at low shear rates by two orders of magnitude, making this an extreme example of shear thinning. A similar effect has been reported by Rahatekar et al.,[28] who used optical observation to associate this remarkable degree of shear thinning with MWNT aggregation. Their conjecture was corroborated by rheo-optical studies reported by other researchers[57, 60] where low shear was observed to induce CNT aggregation or flocculation – as more commonly referred to in the literature of fiber suspensions.[61, 62] It is interesting to note that significant shear thinning behavior can be advantageous to making CNT thin films. Dan et al.[63] prepared various CNT-surfactant solutions with different extents of shear thinning. They found that CNT-surfactant solutions with larger shear thinning effects formed films with more uniform thickness in a roll-coating process, which can be explained by a rapid increase in the viscosity right after the coating process. This effectively slowed down the dewetting process, since the dewetting velocity is inversely proportional to the (zero-shear) viscosity of the coating solutions.

In the case of dilute CNT suspensions, a plateau in viscosity is sometimes observed at low shear rates, and from the plateau value – also known as "zero shear viscosity" (η_0), one can estimate the average length and length distribution[64]. In the classical theory of dilute rigid-rod suspensions[54, 55, 65, 66], the "*intrinsic viscosity*" [η] is related to the aspect ratio of the rods through the following expression:

$$[\eta] = \lim_{\phi \to 0} \frac{\eta_0 - \eta_s}{\eta_s \phi} = \frac{8}{45}\left(\frac{L}{D}\right)^2 \varepsilon f(\varepsilon) \qquad (3)$$

with $\varepsilon = \left[\ln(2L/D)\right]^{-1}$ and $f(\varepsilon) = \frac{1+0.64\varepsilon}{1-1.5\varepsilon} + 1.659\varepsilon^2$, where η_s is the viscosity of the suspending medium, ϕ is the volume fraction, *L* is the length, and *D* is the diameter of the rods.

If the diameter is known *a priori*, then the length of the rods can be calculated from the shear viscosity data. However, the original theory for Brownian rod systems is developed for rods that are monodisperse in both length and diameter. Although the variation in diameter can be assumed to be small, there usually exists a certain length distribution that is not negligible. For this reason, Parra-Vasquez et al. replaced the length in Eqn (3) by a "viscosity average length" defined as:[64]

$$L_{visc} \equiv \sqrt{\frac{\langle L^3 \rangle}{\langle L \rangle}} \qquad (4)$$

where $\langle L \rangle$ and $\langle L^3 \rangle$ are the first and the third moments of the length distribution, respectively.

By fitting eqns 3-4 to experimental data, the authors obtained reasonable agreement, with a 10 – 30% difference between the aspect ratio deduced from rheological measurements and that deduced from atomic force microscopy (AFM) measurements.

Although it is widely accepted that CNT aspect ratio affects suspension rheology, there are surprisingly few studies focusing on this topic in any detail[67, 68]. Fan and Advani[68] reported that "short" CNTs modified the rheology to a lesser extent as compared to "long" CNTs. It should be noted, however, that in their study, "short" CNTs were shortened by chemically treating the CNTs in a mixture of sulfuric and nitric acids, which is also known to modify surface interactions between CNTs and will thus influence the rheology.[41,59] It is therefore highly probable that their experimental results reflect the combined effects of chemical treatment and aspect ratio. Rahatekar et al.[66] prepared two sample batches with different CNT lengths by sonicating one of the samples. The two samples were originally from the same production batch and thus share the same diameter distribution with an average diameter of 50 nm. In terms of length, the "short" CNTs have a length of 5 µm versus the "long" CNTs with a length on the order of 60 µm. In their steady shear measurements, the yield stress showed a dependence on aspect ratio, which the authors proposed to be related to the deformation mechanism as strain is applied to the system. By visualizing the deformation of networks comprised of either long or short CNTs, the authors concluded that individual CNTs tend to act as the load-bearing element in long CNT systems whereas CNT aggregates tend to bear the load under deformation in short CNT suspensions.

Davis et al.[30] used a scaling analysis to show that viscosity-shear rate data for different concentrations of semi-dilute CNT suspensions can collapse into a master curve when the data are re-plotted using the "*reduced viscosity*", which is defined as:

$\eta_r = (\eta - \eta_s)/\eta_s\phi$, where η is the suspension viscosity.

As shown in Fig. 5.4, the slope was found to be -0.5, consistent with the calculations of Kirkwood et al.[65,69] The authors of this paper note that a similar slope was observed in other systems of semi-dilute (non-aggregating) CNT suspensions[56, 64] although the suspending medium and base viscosity are different.

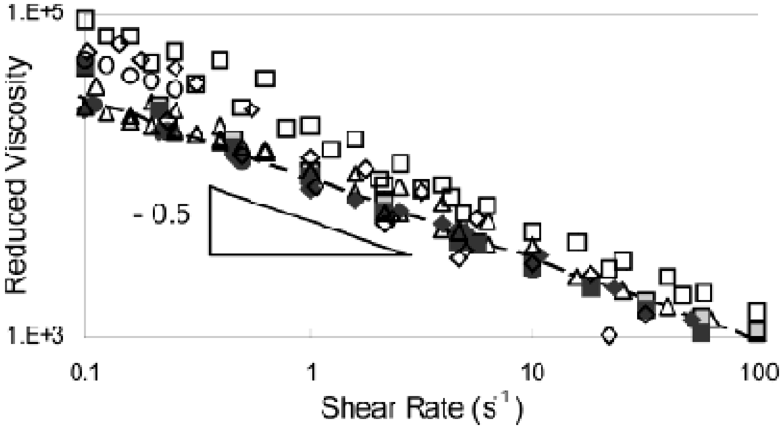

FIGURE 5.4
Reduced viscosity (η_r) versus shear rate for various concentrations (94 – 452 ppm) of SWNTs in chlorosulfonic acid. All the data collapse reasonably well onto the dotted line with a slope of -0.5. η_r is defined as: $(\eta - \eta_s)/\eta_s\phi$, where η_s is the solvent viscosity and ϕ is the volume fraction of SWNT. Reproduced from [30]

Small Amplitude Oscillatory Shear Flow – Linear Viscoelastic Measurements

Most complex fluids are neither purely viscous nor purely elastic, but instead show both viscous and elastic characteristics, termed "viscoelasticity", when subjected to deformation.[70] Viscoelasticity can be measured experimentally by applying oscillatory shear deformation to the sample, where the applied strain (γ) is a sinusoidal function of time[55, 70]:

$$\gamma = \gamma_0 \sin \omega t \tag{5}$$

where γ_0 is the maximum strain amplitude and ω is the angular frequency. The shear stress is then measured and can be expressed in the following form:

$$\tau(t) = \gamma_0 G' \sin\omega t + \gamma_0 G'' \cos\omega t \tag{6}$$

Dividing the stress component that is in-phase with the strain by the maximum strain amplitude gives the "elastic" or "storage" modulus (*G'*), whereas the component that is out-of-phase leads to the loss modulus, usually denoted by *G"*. *G'* and *G"* are measured as a function of frequency and strain amplitude, and the results provide insight into how a material would behave under certain time scales of deformation. The relaxation times of typical liquids vary considerably from ~10^{-12} s for water to ~10 s for polymer melts. For small strain amplitudes, *G'* and *G"* are usually independent of γ_0 and this is also known as the "linear viscoelastic region".

Most of the early experimental studies on the rheology of CNT suspensions focus on their linear viscoelastic (LVE) properties[27]. For instance, Hough et al.[33] measured stress as a function of strain (γ_0) for surfactant-stabilized CNT suspensions. They found that experimental data for different CNT concentrations can be scaled onto a single master curve by assuming a weakly interconnected network which is destroyed at large strains. Their scaling analysis also suggested that the elasticity of the CNT suspensions was a result of weak interactions between surfactant-stabilized nanotubes and was not due to the bending or stretching of CNTs. Nevertheless, whether such scaling analysis is universally true for all CNT suspension systems has yet to be tested.

For a fixed strain within the linear viscoelastic region, Fig. 5.5 shows a typical plot of *G'* and *G"* versus frequency (*ω*) for different CNT concentrations[59]. As the concentration increases, both *G'* and *G"* increase in magnitude and beyond a certain value, a plateau is usually observed at low frequencies, indicating the presence of a physical network.[27, 59, 71] One can use this information to identify the percolation threshold - the critical concentration above which CNTs start to connect and form a space-filling network.[70] The rheological percolation threshold deduced from rheological studies is termed the "rheological or mechanical percolation threshold" and may differ from the "electrical percolation threshold".[31, 72] The rheological percolation threshold can also be measured experimentally from stress relaxation after the application of a step strain.[27, 59]

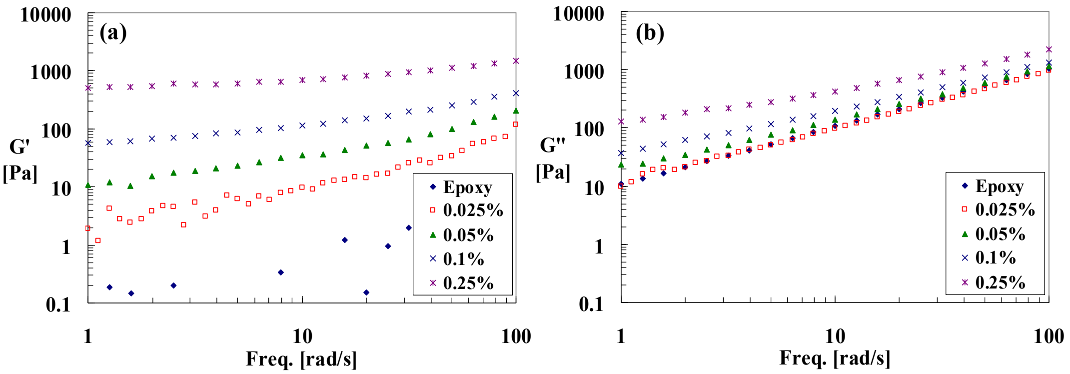

FIGURE 5.5

Dependence of (a) *G'*: storage modulus and (b) *G"*: loss modulus, on the concentration of (as-produced) MWNTs (d: ~ 50 nm; L: ~ 30 µm). Addition of the MWNTs increased both the values of *G'* and *G"*. Strain = 1%. Temperature = 25°C. The MWNTs were produced by the chemical vapor deposition (CVD) method[149] and supplied by the Department of Materials Science and Metallurgy, University of Cambridge. Reproduced from [59]

In principle, the microstructure and viscoelastic response of CNT suspensions are closely related,[29, 31, 68] and LVE data can therefore be used to assess the mixing quality of CNT suspensions. A number of researchers have prepared samples with different mixing quality and performed LVE measurements.[29, 31, 37, 68] However, there has been disagreement on whether better dispersion should lead to a higher *G'* and a *G'* plateau at low frequencies. As pointed out elsewhere[27, 68] the disagreement is probably a result of the existence of different microstructures in these studies. Although the rheological response of CNT suspensions is related to the dispersion state, a *G'* plateau is merely an indication of a physical network. This does not necessarily imply good mixing, because a poorly dispersed sample containing interconnected CNT aggregates will also result in a low-frequency *G'* plateau. Indeed, a more robust way of assessing mixing quality from LVE data was reported by Huang et al.[73], who sampled the LVE response as a function of mixing time. They discovered that the magnitude of complex viscosity (defined as: $\eta^* = \sqrt{\left(G'^2 + G''^2\right)} / \omega$) only reached a steady value when the actual mixing time exceeded a certain critical mixing time that scales linearly with CNT concentration. For their setup and highly-entangled samples, a mixing time of several hours was generally required for establishing a stable rheological response and decent mixing quality.

Some scaling analysis[74] can be applied to the LVE data of CNT suspensions as demonstrated by Hobbie and co-workers.[67, 75] By scaling both *G'* and *G"* with a linear viscoelastic shear modulus, $\kappa(\phi)$, which is essentially the low *G'* plateau value, and the frequency by a characteristic relaxation time $\left(\tau = \eta_0 / \kappa\right)$, LVE data for different concentrations of CNT collapsed onto a single master curve (Fig. 5.6). As shown in the figure, the scaled LVE response of long CNTs matches very well with that of short CNTs at a moderately higher concentration, indicating a universal scaling form in terms of the shear moduli.

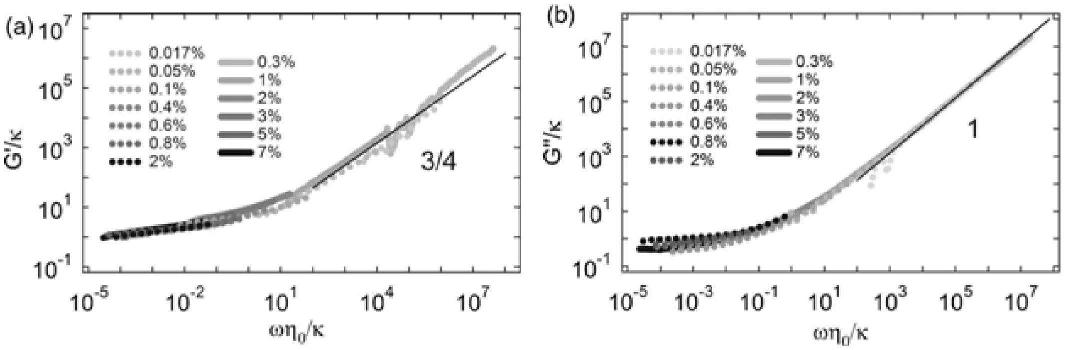

FIGURE 5.6

(a) *Scaled* storage modulus and (b) loss modulus for short (solid) and long (dashed) MWNTs. κ and η_o / κ are the scaling factors for the moduli (*G'* and *G"*) and frequency (ω) respectively. The low-frequency *G'* plateau reflects the linear elasticity of the CNT network and the overlap of data for long and short MWNTs indicate a universal form for the scaled linear viscoelastic response. Reproduced from [67]

Extensional flow

Extensional rheology is highly relevant to a number of processes such as fiber spinning[49], inkjet printing[76] and curtain coating.[77] The extensional rheology of CNTs suspended in a Newtonian fluid has been studied experimentally by Ma et al.[78] and later by Tiwari[79] using the technique of liquid filament thinning.[80-84] In a typical filament thinning experiment, a liquid thread is first formed between two endplates by stretching the CNT suspensions simultaneously in opposite directions, as shown in Fig. 5.7I. Upon cessation of stretching, the liquid filament starts to thin (decrease in diameter) and undergo uniaxial elongation as a result of surface tension. The way the liquid filament thins and the time required for filament breakup depend on the interplay between surface tension, viscous, and elastic forces. From the filament thinning profile, one can obtain useful information about the extensional flow behavior and in some cases the extensional viscosity of the testing fluid.

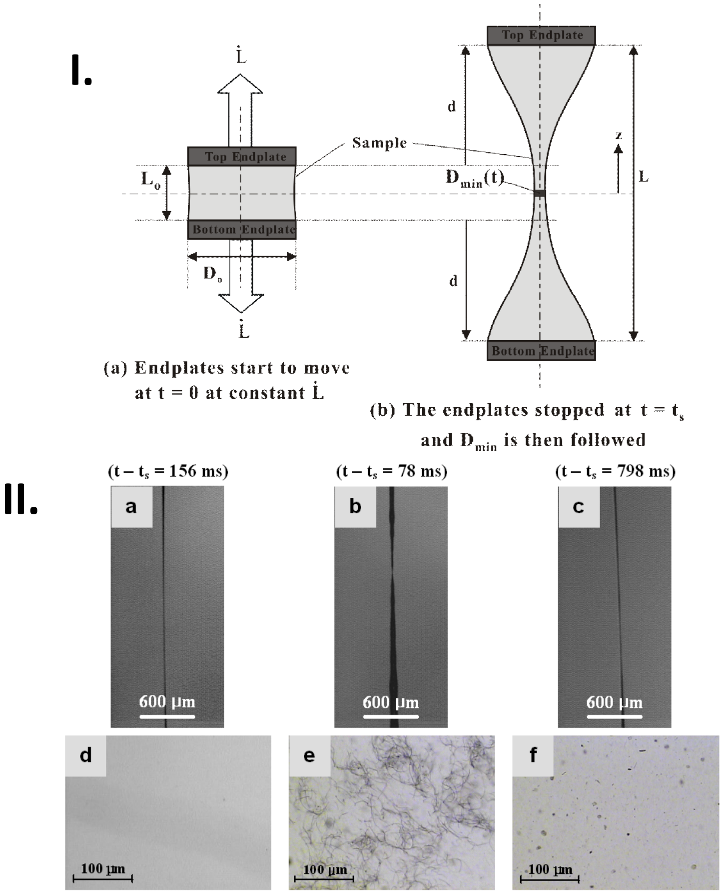

FIGURE 5.7
I. Schematic diagram of a filament thinning experiment showing top and bottom cylindrical endplates and fluid contained between the endplates for (a) the initial condition (t = 0) and (b) an arbitrary later time t. Adapted from [78].II. Figs. (a) – (c) show the filament profile before breakage for (a) epoxy, (b) an aggregating CNT suspension, and (c) anon-aggregating suspension of functionalized CNTs. Figs. (d) – (e) show corresponding optical micrographs captured using the Cambridge Shear System (CSS450, Linkam Scientific Instruments) with an optical depth of 130 μm. t_s is the time at which the endplates stopped. Reproduced from [78]

Ma et al.[78] carried out filament thinning experiment on two CNT suspensions showing completely different optical microstructures (Fig. 5.7II). One of the suspensions showed optically resolvable aggregates with a size on the order of ~100 microns (Fig. 5.7.II.e), while the CNTs in the other suspension were functionalized to prevent aggregation (Fig. 5.7.II.f). Liquid filaments formed from the CNT aggregate suspension tended to thin in a non-uniform way (Fig. 5.7.II.b) and break prematurely. Irregularity of the filament along its axial direction is consistent with the presence of CNT aggregates and reliable data on extensional viscosity cannot be obtained because of the irregularity and poor reproducibility inherent to such a non-homogeneous sample. In the case of non-aggregating suspensions, the addition of CNT prolonged the breakup time significantly and the extensional viscosity of the non-aggregating CNT suspensions was subsequently estimated from the capillary thinning data.[85, 86] The enhancement in extensional viscosity agreed reasonably well with the theoretical predictions of Batchelor[87] developed for (aligned) rigid-rod suspensions. It is worth noting that a similar effect has been reported for glass fiber suspensions[88]. Intuitively, the increase in breakup time can be explained by the flow-induced orientation of CNT towards the stretching direction, which in turn increases the total stress and resists further deformation. Based on the CNT orientation argument and a Fokker-Planck orientation model,[56] the authors estimated a high degree of CNT alignment (99%) after an initial strain input of 5 strain units[89].

Using a similar filament thinning technique, Tiwari et al.[79] studied the effects of CNT concentration, CNT aspect ratio, the base viscosity of the suspending medium, and the initial diameter of the liquid thread on the extensional flow behavior of CNT suspensions. The authors observed that liquid filaments tended to break in a non-Newtonian way for suspensions with higher CNT concentration, larger CNT aspect ratio, and higher suspending medium viscosity. For the high concentration samples, there existed a critical diameter above which the liquid filaments did not undergo capillary thinning – an effect the authors attributed to the presence of yield stress in CNT suspensions. The authors applied the Herchel-Bulkley (HB) model for power-law fluids with a yield stress to model the CNT suspensions in shear and extensional flows. There is good agreement between two of the model parameters obtained from extensional flow and shear data respectively, but the yield stress – the third parameter in the model – deduced from extensional flow data was found to be 40% higher than that obtained from the shear data fitting. The author suggested that the discrepancy might be resolved by using a modified HB model where the yield stress is allowed to vary depending on the type of flow.

Highly Concentrated Regime and the Formation of Liquid Crystalline Phases

As in the case of other rigid rod systems such as tobacco mosaic virus[90], CNTs can form liquid crystalline phases [91, 92] at sufficiently high concentration levels. The distinguishing characteristic of the liquid crystalline state is the tendency of the molecules (mesogens) to point along a common axis, called the director. This is in contrast to molecules in the liquid phase, which have no intrinsic order. In the solid state, molecules are highly ordered and have little translational freedom. The characteristic orientational order of the liquid crystal state is between the traditional solid and liquid phases and this is the origin of the term mesogenic state, used synonymously with liquid crystal state.

In this section, we highlight some of the CNT systems that show liquid crystalline phases, followed by discussions on some of the rheological characteristics of liquid crystalline solutions of CNTs in superacids. For carbon nanotubes, however, such liquid-crystalline order can often be preempted by the formation of a disordered isotropic gel. The absence of liquid crystalline order in some of these suspensions can be attributed to a number of factors. Attractive interactions and length polydispersity both act to extend the biphasic region of the phase diagram. Similarly, the attractive interactions that are ubiquitous in many surfactant-based carbon nanotube suspensions can serve to inhibit the onset of complete nematic ordering by promoting gelation, which effectively traps the suspension in a disordered metastable state. Although morphologically similar to the analogous isotropic phase in the semi-dilute regime, the higher yield stress of these suspensions will render them virtually unprocessable with flow.

Experimental observations of CNT liquid crystalline phases

Non-functionalized CNTs in "superacids"

In general, dispersing CNTs in ordinary fluids without the aid of surfactant or functionalization has proven to be extremely difficult. However, it has been demonstrated[30, 48, 49, 93, 94] that CNTs are soluble in the "superacids", such as fuming sulfuric acid or chlorosulfonic acid. This method of dissolution has opened up significant opportunities, including the preparation of stable CNT suspensions at high concentrations, the formation of CNT films,[95,96,97] and the spinning of neat CNT fibers [49,50,98]– similar to the way in which Kevlar® and Zylon® fibers are spun. Over the past years, some basic understanding about the dissolution mechanism and phase behavior of such systems has been established. In essence, CNTs are rendered soluble in superacids via the protonation of the CNT sidewall, which subsequently leads to an electrostatic repulsion between nanotubes[48, 94]. The process was found to be reversible and the integrity of the sidewall was preserved according to Raman spectroscopy data.[48] Different CNT-superacid mixtures were prepared using different CNT concentrations and superacids with varying acid strength, as measured experimentally by Raman shift). An experimental phase diagram (Fig. 5.8) was then constructed for CNT-superacid systems,[99] where the isotropic, biphasic, and the liquid crystalline regimes were identified. The biphasic regime is the regime where an isotropic phase co-exists with a liquid crystalline phase. To quantify the amount of CNT present in the isotropic phase, these mixtures were centrifuged and the concentration of CNT in the isotropic phase was measured using UV-vis-NIR absorbance.[93] There are two interesting observations. First, the isotropic to biphasic boundary shows a stronger dependence on SWNT protonation, as compared to the biphasic to liquid-crystalline boundary. Second, the biphasic regime is much broader than that predicted by the classical theories of Onsager[100] and Flory[101] and the authors attributed this to the polydispersity of the SWNTs. In terms of modeling the phase behavior of CNT-superacid solutions, Green et al.[47] adopted a polydisperse rigid rod model developed by Wensink and Vroege[102], which is an extension of the Onsager theory[100] for monodiperse rods. Furthermore, the authors postulated that in the CNT-superacid system, there exists a competition between short-range repulsion (due to protonation) and long-range van der Waals attraction. Their postulate was inspired by experimental observations of long threadlike liquid crystalline structures termed "spaghetti" (Fig. 5.8.II) that are sometimes found in fuming sulfuric acid systems. The authors assumed a phenomenological square-well potential where the depth of the attractive well varies as a function of solvent quality (acid strength)[47]. The theoretical model agrees very well with the experimental broadening of the biphasic regime in the phase diagram, further supporting the postulate about the nature of CNT interactions.

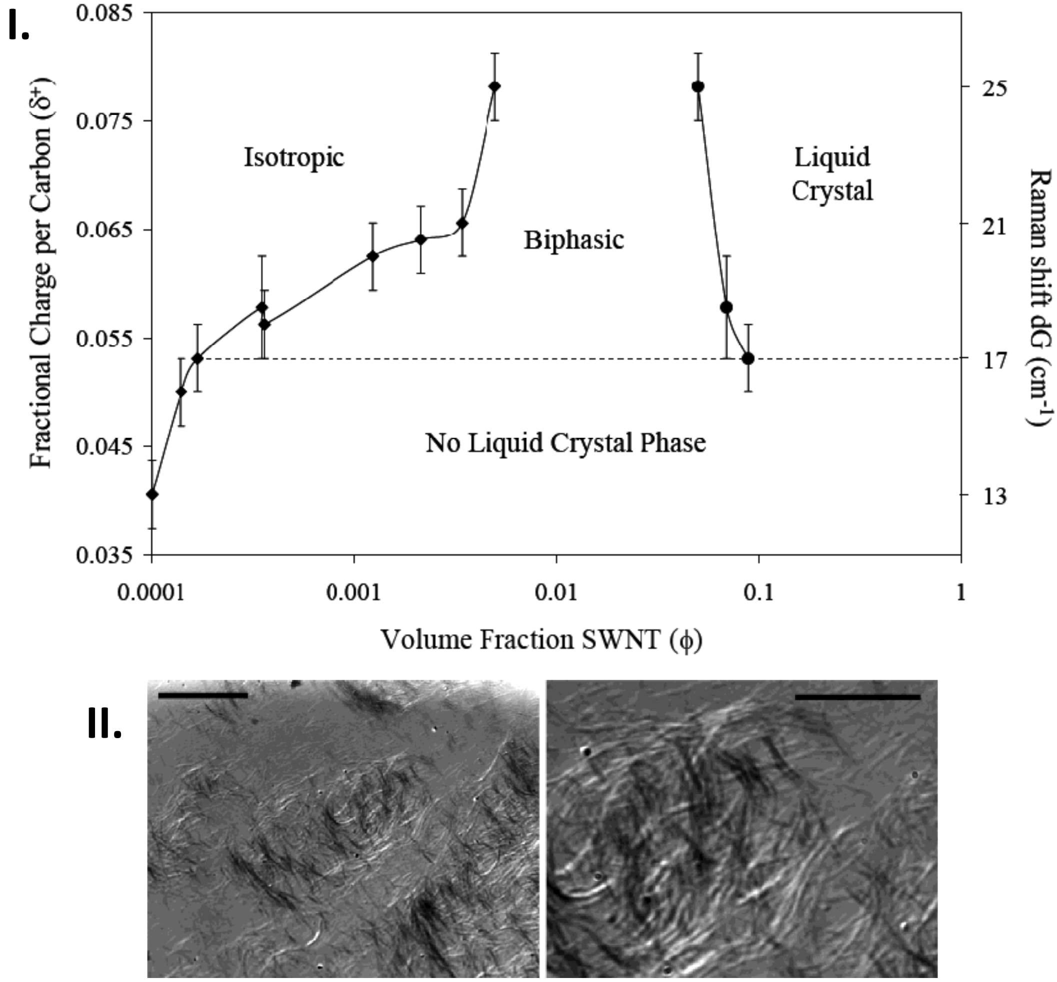

FIGURE 5.8
I. Phase diagram for SWNTs in superacids. The isotropic to biphasic boundary shows a stronger dependence on SWNT protonation, compared with biphasic to liquid crystalline boundary. Below a critical level of protonation ~ 0.053 fractional charge per carbon, SWNTs do not disperse well enough to form a liquid crystalline phase. Adapted from[99]. II. Formation of spaghetti-like liquid crystalline structures in 0.32% (vol) solution of SWNTs in 102% sulfuric acid. The scale bar of the image on the left is 20 µm and that on the right is 10 µm. Reproduced from [30]

Oxidized CNTs in water

Windle and co-workers[103] oxidized the CNTs using a mixture of concentrated sulfuric acid and nitric acid and dispersed them in water. They observed the formation of nematic liquid crystalline phases at concentration above 4.3% (vol). Following on their initial observations, Song and Windle[104] applied reflected polarized light microscopy to systematically study the phase transition of aqueous suspensions of oxidized CNTs as a function of concentration. For CNT concentrations as low as 1.3% by volume, they observed the presence of “nematic nuclei” (Fig. 5.9a, b) which grow in size and form “nematic swarms” (Fig. 5.9c) as the CNT concentration increases. These nematic swarms started to join up and finally form the typical Schileren texture of nematic liquid crystalline phases at a concentration of 5.3% (Fig. 5.9d). As in the case of CNT superacid systems, they noted that the biphasic regime was much wider than that predicted by Onsager[100] and Flory[101] theories. Similarly, the authors attributed the widening of the biphasic “chimney” to the polydispersity of the samples.

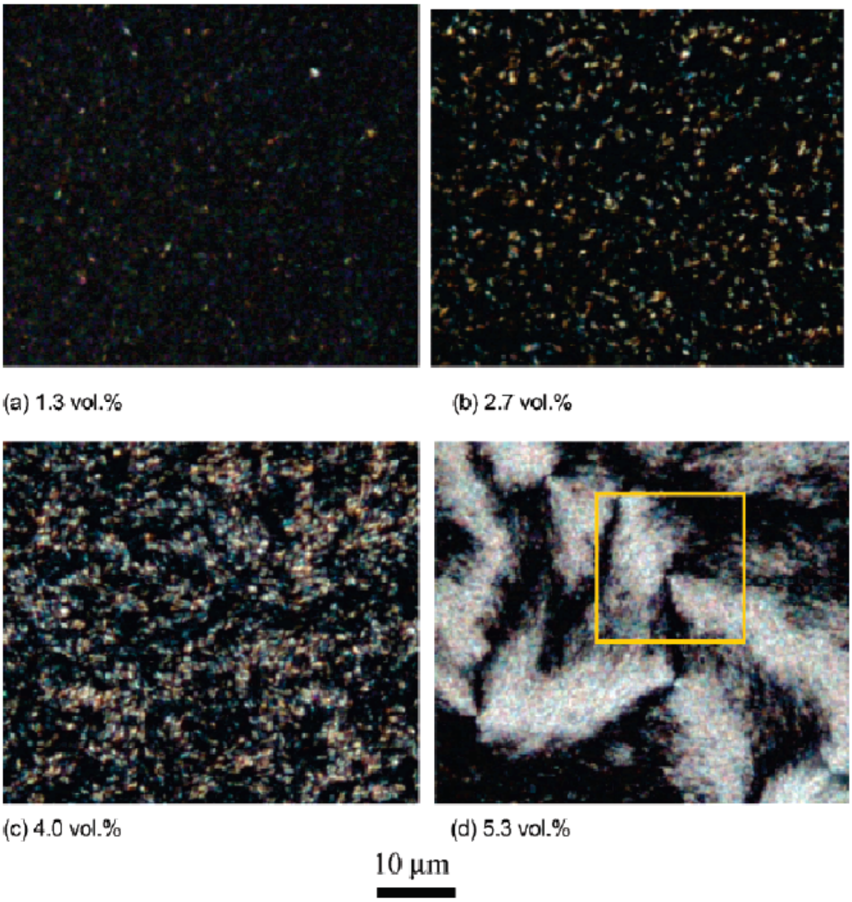

FIGURE 5.9
Reflected polarized light micrographs of oxidized MWNTs dispersed at different concentrations in water (a) 1.3% (vol), showing weak bireflection from “nematic nuclei”; (b) 2.7% (vol), where the nematic nuclei appear to be larger; (c) 4% (vol), where some of the nematic nuclei start to join up, forming “nematic swarms”; (d) 5.3% (vol), showing Schlieren texture of nematic liquid crystals. Reproduced from [104]

In a later paper, Song and Windle[105] studied the effect of initial CNT size (diameter and length) on liquid crystalline texture in greater detail (Fig. 5.10).

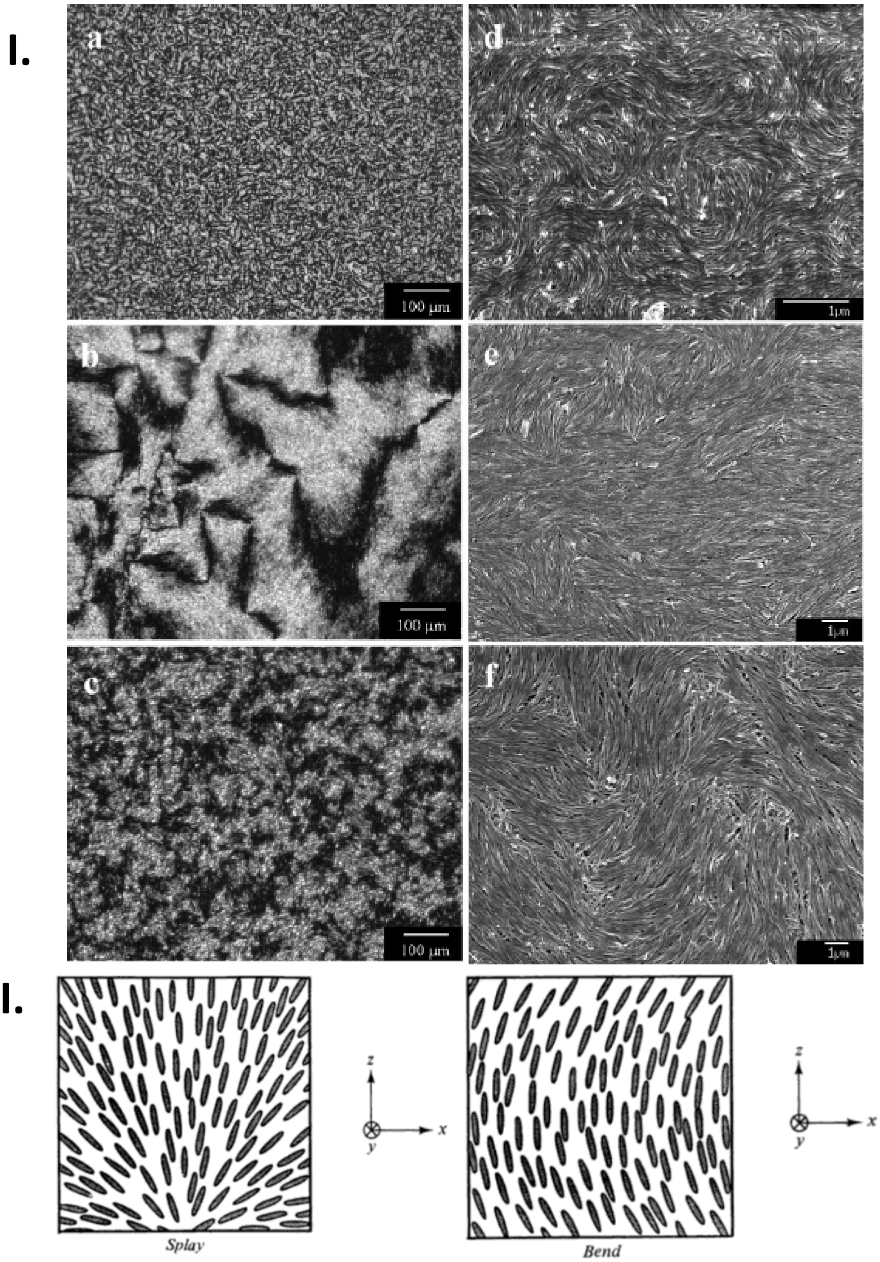

FIGURE 5.10
I. Figs. (a)-(c) Optical microscopy and SEM images of nematic dispersions prepared from different sizes (diameter and length) of oxidized MWNTs. Figs (a) and (d): “short and thin” MWNTs; Figs. (b) and (e): “short and thick” MWNTs; Figs. (c) and (f): “long and thin” MWNTs. Adapted from [105]. II. Schematic diagrams of “splay distortion” and “bend distortion” commonly observed in liquid crystalline polymers. Reproduced from [106]

Cross-polarized reflected-light microscopy clearly showed that the liquid-crystalline texture depends strongly on the length as well as the diameter (and thus flexibility) of the CNTs. Three different samples were investigated (Fig. 5.10.I) and as the sample is confined within a small gap, only two types of orientational distortion are considered (as illustrated in Fig. 5.10.II). The authors argued that “splay distortion” is more energetically favorable than “bend distortion” in the case of “short and thick” CNTs. Conversely, “bend distortion” is favored in the cases of “short and thin” and “long and thick” CNTs because flexibility allows the CNTs to bend to follow the curvature around defect cores, as evidenced in the SEM images of dried samples.

DNA-stabilized CNTs in water

Although CNTs have been widely dispersed in water with the aid of surfactants, increasing the concentration of nanotubes in these systems does not necessarily result in the formation of a nematic liquid crystalline phase[92]. With only a few exceptions[107], CNT tends to form isotropic aggregates at high concentrations, an effect that is probably enhanced by the presence of surfactant micelles, which at sufficient concentrations result in depletion attractions between CNTs. Badaire and co-workers[108] managed to induce the formation of liquid-crystalline phases in aqueous suspensions of DNA-stabilized CNTs. The authors suggested that unlike low-molecular weight surfactants, denatured DNA strongly adsorbs onto the CNTs and therefore can be effective at sufficiently low concentrations such that it does not induce a depletion attraction. In their study, they observed a transition from an isotropic phase to bi-phasic and subsequently to a nematic phase as they increased the solute (DNA-CNT) concentration by evaporating the aqueous solvent. A phase diagram was presented (Fig. 5.11) and, similar to the CNT-superacid and oxidized CNT system, the experimental biphasic region was wider than that predicted by classical theories for mono-dispersed rigid rod systems[100, 101]. The authors attributed this to the polydispersity of the CNT bundles, as confirmed in their depolarized dynamic light scattering studies.[109]

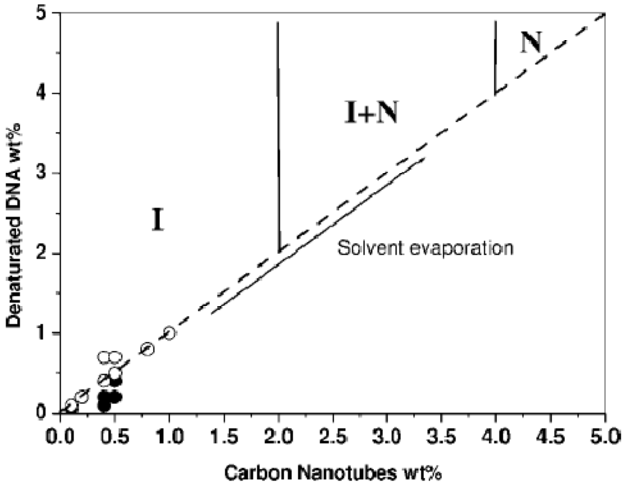

FIGURE 5.11
Phase diagram of DNA-stabilized CNT bundles in water. The dashed line indicates the limit above which the CNTs are homogeneously dispersed after sonication (white circles). Below the line, aggregates are still observable (black circles). The systems were concentrated to levels greater than 4wt% by solvent evaporation. This method allowed the concentrations of the DNA and CNTs to increase proportionally. In the domain of homogeneously stabilized CNTs, the system forms an isotropic (I) phase at concentrations below 2wt%, and a nematic (N) phase above 4wt%. A coexistence of the phases (I+N) is observed in between these boundaries. Reproduced from [108]

CNTs in N-isopropyl acrylamide gel

Islam et al.[110] created a nematic CNT gel by first dispersing CNTs, with the aid of the surfactant NaDDBS, in a solution of isopropyl acrylamide monomer. The monomer was then cross-linked to form a gel. For an initial CNT concentration < 1.34 mg/ml, the CNTs trapped within the gel tended to be isotropic, but the gel was then subjected to high temperatures where the gel became hydrophobic and expelled water. Although there was still water in the sample after the treatment, the volume was decreased by nearly an order of magnitude and the CNT concentration increased substantially as a result. Using this method, gels with CNT concentration as high as 8.25 mg/ml were prepared. Clear birefringence evidence was observed and the Scalar order parameter (S) was estimated from polarized light microscopy. *S* value as high as 0.8 was reported for areas close to the edge of the gel, while the bulk of the sample showed a much lower degree of alignment with *S* = 0.4 (see also section 5.3). Caution should be taken, however, in referring to absolute values of *S*, as in calculating the scalar order parameter a stretched sample is used as a reference of complete alignment (i.e., *S* = 1). In both the edge and bulk of the sample, an abrupt change in the scalar order parameter was observed at a concentration of 3.3 mg/ml, which the authors identified as the critical concentration for the isotropic-nematic transition. Additionally, it is interesting to note that the gel buckled after shrinkage and the authors attributed this to the difference in the degree of alignment between the edge and the bulk of the sample, as in the case of some thermotropic nematic elastomers that tend to exhibit strain along the direction of nematic order.

Rheology

The rheology of liquid-crystalline CNT suspensions is, in general, not as well studied as for other liquid crystal systems. This may be due to the fact that not all CNT systems can form liquid crystalline phrases; as discussed in the previous section, CNT-surfactant suspensions, for example, tend to form isotropic aggregates at high concentrations. Another possible reason is that as in the case of other highly concentrated suspensions, it is generally more challenging to measure accurately and reproducibly the rheology of CNT liquid crystalline systems due to high particle concentration levels. The relaxation time in these suspensions can be so long that the effect of previous shear history is not negligible.[70, 111] In other words, the sample “remembers” shear stress that is (inevitably) created during sample preparation and loading. Although strong pre-shearing can be applied to “override” the memory of shear history prior to rheological measurement, obtaining reliable data on the rheology of highly concentrated CNT suspensions is difficult and requires considerable care.[70, 111]

The rheology of oxidized CNTs in water[41] was published before another publication[103] by the same group reporting liquid crystallinity. Although in the earlier rheology paper[41] there was no mention of liquid crystalline phases, we note that their rheological results cover a wide range of concentration, from 0.4 vol % to as high as 9.2 vol %. The data of highly concentrated oxidized CNTs might also be of relevance. However, in this section, we will focus on the work of Davis and co-workers[30] on the rheology of liquid-crystalline CNTs in superacid, where polarized light microscopy shows clear evidence of liquid crystallinity. The characteristic rheological signatures of liquid crystalline solutions, the steady and transient shear viscosity and the first normal-stress difference, will be discussed in the context of CNT suspensions.

Steady and Transient Shear Viscosity

Davis et al.[30] measured the steady shear rheology of CNTs suspended in 102% fuming sulfuric acid (with 2 % excess SO_3). When they plotted the (low) shear viscosity as a function of CNT concentration (Fig. 5.12a), the results showed remarkable resemblance to those of liquid crystalline polymers (Fig. 5.12b)[112]. At low concentrations, the suspension viscosity increased as a function of increasing concentration until a maximum viscosity of ~1100 Pa s at around 3.5 vol %. The viscosity then decreased immediately after the maximum and finally increased again at still higher concentration. Their rheological data suggested a transition from a biphase to a single nematic liquid-crystalline phase between 3.5 and 5.1 vol %. Evidence for the transition is supported by polarized light microscopy, where a polydomain liquid crystal was observed at 5.1 vol %. It is worth noting that the nematic phase of CNTs in fuming sulfuric acid also showed a viscosity curve with some resemblance to that of a nematic LCP.

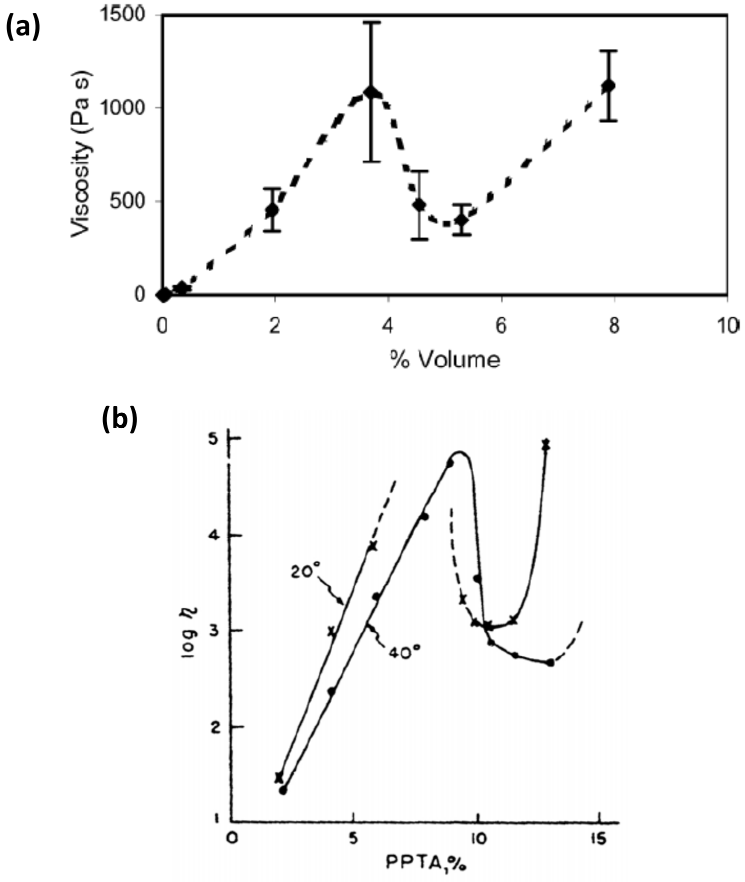

FIGURE 5.12
(a) Shear viscosity as a function of SWNT concentration in 102% sulfuric acid (2% excess SO_3) for a shear rate of 0.1s^{-1}. Transition from a biphase to a single nematic liquid crystalline phase occurs between the maximum at ~3.5% (vol) and the minimum at ~5.1% (vol). Error bars represent standard deviation in measurements for at least 3 samples. Adapted from [30]. (b) Viscosity versus concentration of poly-paraphenylene terephthalamide (PPTA) in sulfuric acid (for a shear stress of 2x10^3 dyne/cm^2). Reproduced from [155, 156]

As shown in Fig. 5.13, there exist three regimes in the shear viscosity vs. shear rate data: at low shear viscosities, the solution shear thins as shear rate increases (Region I). This is then followed by a second region where the viscosity is almost constant with shear rate (Region II). Finally, at still higher shear rates, the solution exhibits shear thinning again (Region III).

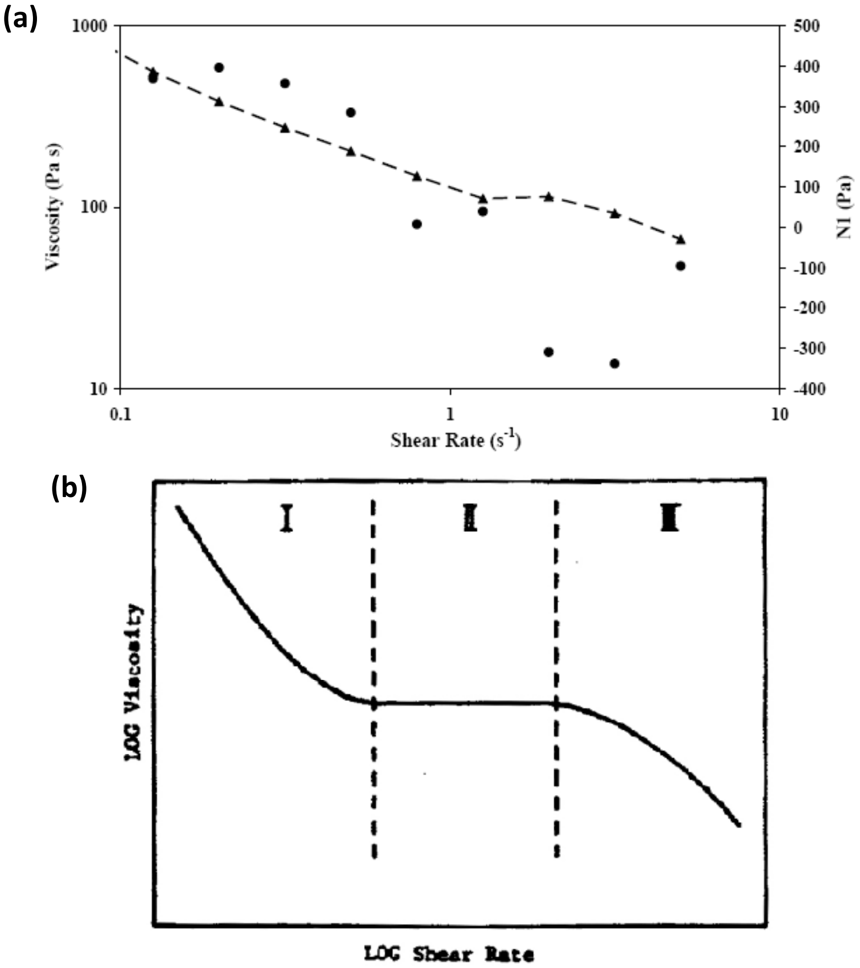

FIGURE 5.13
(a) Viscosity (triangles) versus shear rate for 4.5% (vol) SWNT in 102% sulfuric acid measured on 25 mm cone and plate (cone angle = 0.04 radians). N1 (circles) is the first normal stress difference, which changes sign as a function of shear rate – a rheological characteristic of some liquid crystalline polymers. Adapted from [99]. (b) Three region flow curve proposed for liquid crystalline polymers. Reproduced from [117]

In a typical transient shear experiment, a constant shear rate is applied to the testing sample, and the shear stress (or viscosity) is then measured as a function of time. For nematic solutions of CNT in fuming sulfuric acid, the transient shear stress oscillates as a function of strain (the product of shear rate and time) for more than 100 strain units (as shown in Fig. 5.14). This is yet another rheological signature commonly observed for nematic liquid crystalline polymers (LCPs). In ordinary polymers, these oscillations may also occur but usually disappear after a few strain units.[112]

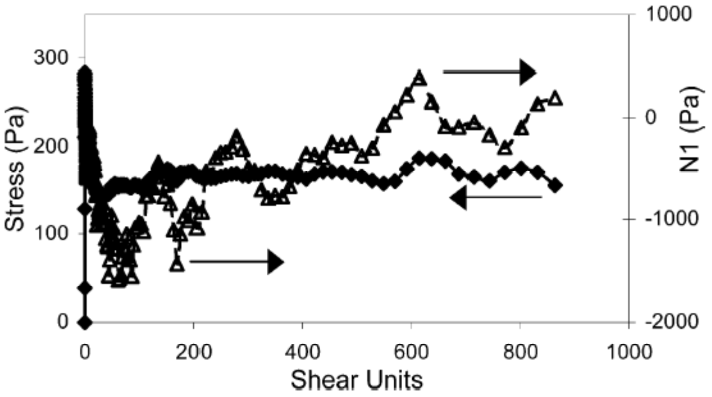

FIGURE 5.14
Transient shear stress and N1 (first normal stress difference) as a function of shear units (= shear rate x time) during start-up flow in 25 mm parallel plates at a shear rate of 5s^{-1}. Solid diamonds represent shear stress and open triangles represent N1. Reproduced from [30]

First Normal Stress Difference

The sign of the first normal stress difference $\left(N_1 = \tau_{xx} - \tau_{yy}\right)$, defined as the difference between the normal stresses perpendicular and parallel to the flow direction, has relevance to the flow processing of complex fluids.[70] For ordinary polymer melts and solutions, a positive normal stress difference is usually measured and is associated with the phenomenon of “die swell” for a polymer extruded out of an orifice[113] (see Fig. 5.15a). However, the opposite was found to be true in some CNT systems (Fig. 5.15b).[30, 40, 114] For liquid crystalline solutions of CNTs in fuming sulfuric acid, a positive N_1 was recorded at low shear rates that decreased as the shear rate is increased. Above a shear rate of 1 s^{-1}, a negative N_1 was measured; as in the case of some lyotropic nematic LCPs, the change in the sign of N_1 coincides with the onset of Region III in the shear viscosity curve. Finally, at even higher shear rates, N_1 in the CNT-superacid liquid crystalline solutions increases again and may or may not reach a positive value beyond the accessible range of shear rate (Fig. 5.14). As Davis et al. explained,[30] the solution usually becomes unstable and expels itself from the gap beyond a shear rate of 10 s^{-1}.

Based on the current understanding of LCP systems, Davis and co-workers[30] conjectured that at low shear rates the suspension tumbles (meaning the director of liquid crystalline nematic domains rotates continuously in flow) which gives rise to the shear thinning observed in region I; at intermediate shear rates (region II), there is a competition between shear-induced alignment and tumbling, resulting in a “wagging” motion. Finally, as shear alignment starts to dominate at higher shear rates, the CNTs align with the flow direction, leading to another shear thinning regime and a positive first normal stress difference. Of course, this conjecture has yet to be confirmed and requires further investigation, for example, by means of in-situ flow visualization. In the literature, a negative first normal stress difference has also been reported for MWNTs suspended in both Newtonian polyisobutylene (PIB)[114] and a non-Newtonian polypropylene polymer melt.[40] The origin for a negative N_1 is unclear and may well be different from the liquid crystalline case. For the latter systems, deformation of CNT clusters, CNT networks, and individual CNTs have been proposed as possible origins.[40, 114]

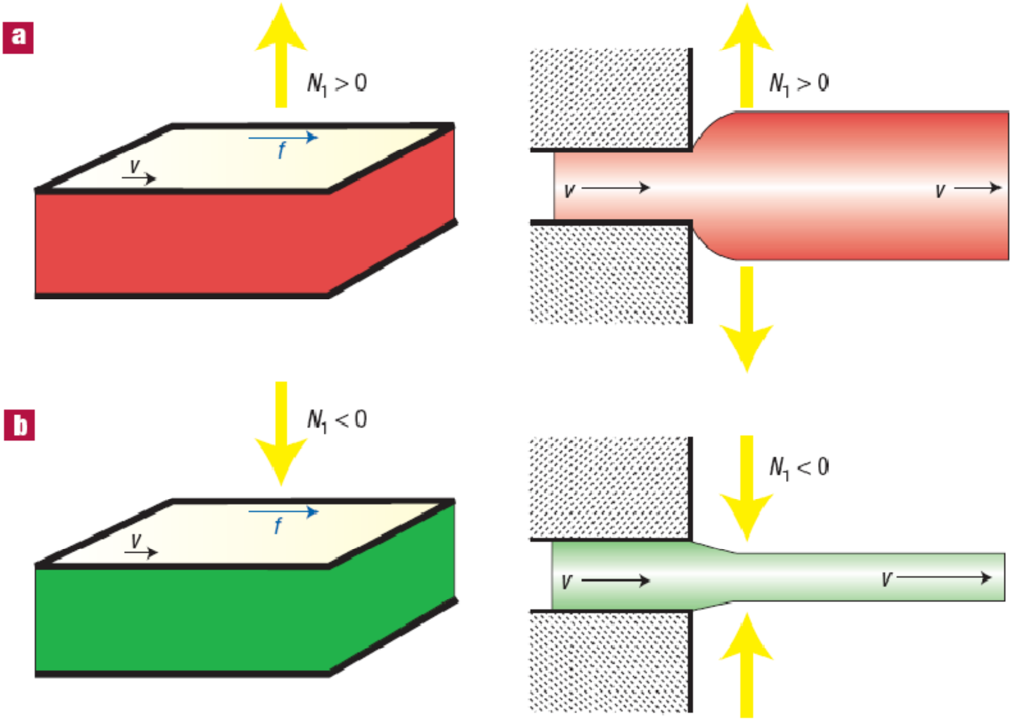

FIGURE 5.15
(a) Generally, when polymer melts are sheared between parallel plates, they develop tensile stresses along the flow direction and compressive stresses in the cross-stream direction. The difference between these stresses N1 is positive and induces a net force that pushes the plates apart (left). In the related extrusion flow (right) the polymer is sheared inside the die and swells when it exits the die. (b) In some CNT systems, a negative N1 occurs, which pulls the plates together (left) and contracts when it exits the die (right). Reproduced from [40]

Understanding rheology from microstructure

Probing the microstructure

Light microscopy

Depending on the actual size of the nanotubes, CNTs can be imaged using light microscopy provided that the length of the nanotube is larger than the diffraction limit of the experimental apparatus. Lin-Gibson, for example, suggested that CNTs with a diameter of as small as 50 nm but a length of 10 µm can be imaged with light microscopy because the CNTs absorb light strongly[114, 115]. It is relatively easy to image CNTs in-situ when the CNTs bundle and/or aggregate into larger optically resolvable structures. The optical microstructure of CNT suspensions during flow can be followed using a flow cell coupled with a light microscope as reported by a number of authors.[28, 39, 89, 114] In cases where SWNTs are dispersed as individual entities, imaging SWNTs has been more challenging but can be achieved using a number of experimental techniques. Fluorescence microscopy, for example, was successfully used to capture the thermal motion of CNTs (in the absence of external flow) with[116] or without[53] the use of fluorescent tagging (see section 2).

X-ray Scattering

Small angle x-ray scattering (SAXS) with a synchrotron source was applied to characterize the in-situ alignment of CNTs during flow.[118] The flow-induced alignment of CNT as a function of increasing shear rate was confirmed by SAXS data. In addition to the flow-vorticity plane, the authors also studied the degree of alignment in the flow-velocity gradient plane, which is less commonly reported in the literature. The authors found that there is a higher level of flow alignment when viewed in the flow-velocity gradient plane. In addition to SAXS, wide-angle x-ray scattering (WAXS) has been used to measure the degree of alignment of MWNTs in composite materials as a function increasing strain, exploiting from the spacing (3.4 Å) between different graphene layers of MWNTs[119].

Polarized Raman Spectroscopy

Raman spectroscopy is one of the most commonly used characterization techniques for CNTs[120-122] and their composites.[123-125] A detailed review of Raman characterization techniques for CNTs is beyond the scope of the current paper; excellent reviews can be found elsewhere.[126] Here we only highlight some of the Raman studies that have been used to characterize the orientation of CNTs in flow. Due to the highly anisotropic geometry of CNTs, the signal intensities of several Raman modes depend on the orientation of the CNT with respect to the polarization of the incident excitation, being maximum when the CNT axis is aligned parallel to the laser polarization.[121, 122] Zamora-Ledezma et al.[125] studied the effect of mechanical shearing on nematic aqueous suspensions of SWNTs stabilized by denatured DNA. Their optical microscopy studies and polarized Raman measurements indicated shear alignment of SWNTs, but the degree of alignment experimentally measured was small (with a typical scalar order parameter of 0.1 – 0.15). The authors attributed this to the waviness of the CNTs, possible CNT entanglement, and viscoelastic effects.

Cryo-TEM and "Post-mortem" Analysis

Cryogenic transmission electron microscopy (cryo-TEM) has been successfully applied to characterize the state of dispersion for CNTs stabilized by various surfactants in water.[127] More recently, this experimental technique has been extended to study CNTs suspended with chlorosulfonic acid, with the results showing that CNTs are dispersed as individual entities at low concentration levels[128, 129] (Fig. 5.16). In addition to cryo-TEM, in cases where the CNTs are suspended within a polymer melt or a matrix that is photo- or thermally curable, "post-mortem" analysis can be carried out using transmission and scanning electron microscopy after rapidly cross-linking the matrix[36, 68, 130, 131] or quenching a thermoplastic.[36, 131] Figure 5.17 shows a series of optical images where the acrylic suspending medium was rapidly cross-linked upon the cessation of rotary shear within a parallel-plate rheometer, to preserve the flow-induced structures formed by various types of CNTs.[59, 130] Technically, such a method can also be used to preserve the orientation of CNTs provided that the rotary relaxation time of the CNTs is longer than the cross-linking/curing time, and provided that the cross-linking process has negligible effect in the orientation distribution [59].

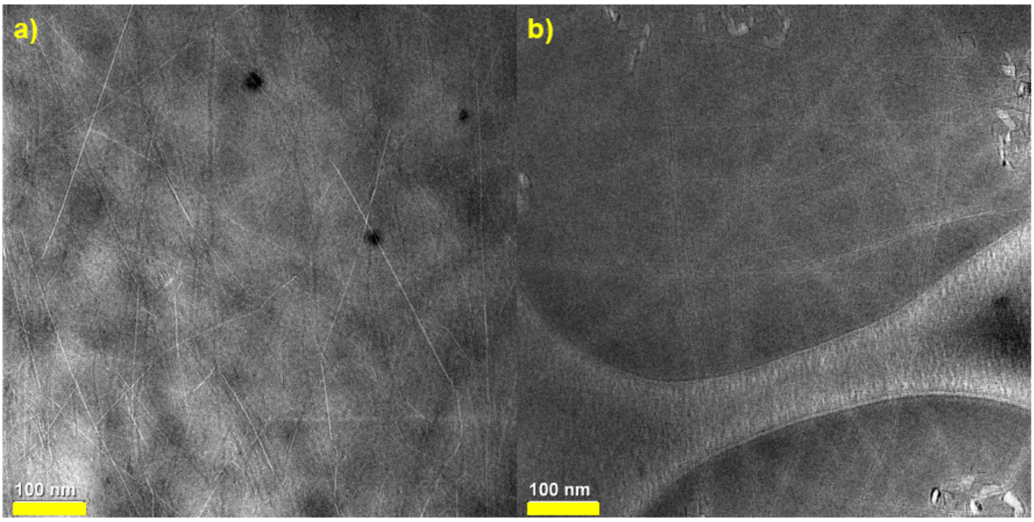

FIGURE 5.16
Cryo-TEM images of a) carpet grown SWNTs and b) Sunnano SWNTs dispersed in chlorosulfonic acid, revealing SWNTs dispersed as individuals. The vitrified chlorosulfonic acid has a higher contrast than the SWNTs, so e-beam irradiation is needed to lighten the acid, making SWNTs visible. The concentrations are 100 ppm and 300 ppm (by mass) respectively. Both scale bars are 100 nm. Adapted from [128]

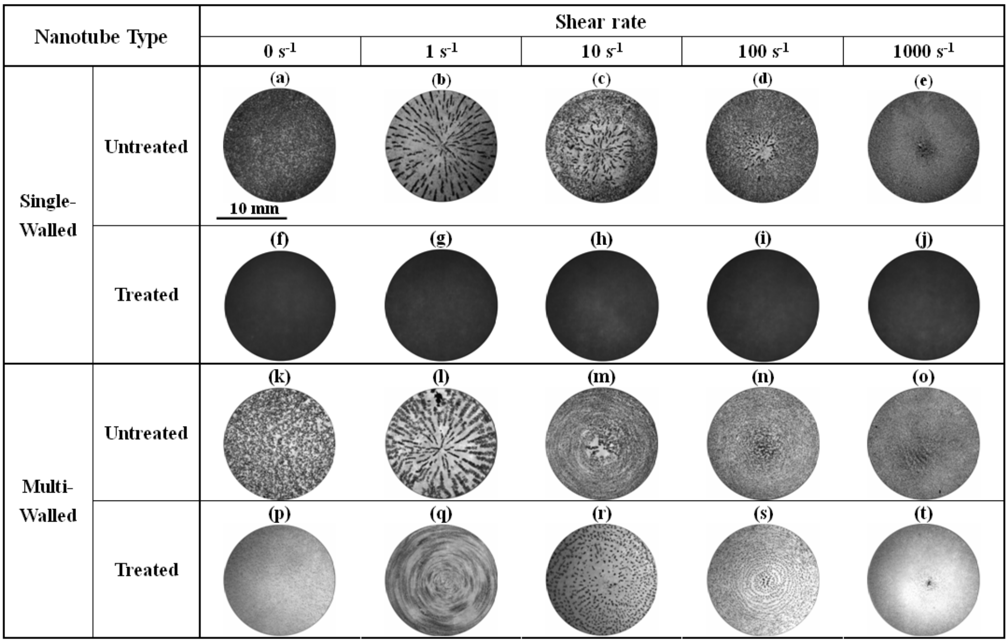

FIGURE 5.17
Optical microstructures of four different types of CNT suspensions where the acrylic suspending medium was rapidly cross-linked upon the cessation of rotary shear within a parallel plate rheometer. Conc. = 0.05%. Optical images were presented as a function of increasing shear from the left to the right with a shear time in excess of 100 s and gap size= 300 µm. Reproduced from [59, 130]

General observations of microstructure evolution in flow

Using experimental techniques described in the previous section, the microstructure of CNT suspensions has been characterized while they were subjected to different strengths of shear flow. As illustrated in Fig. 5.18, flocculation or shear-induced aggregation tends to happen at low shear rates[57, 89, 109] especially in case of (weakly) attractive, or "sticky", CNTs.[39]

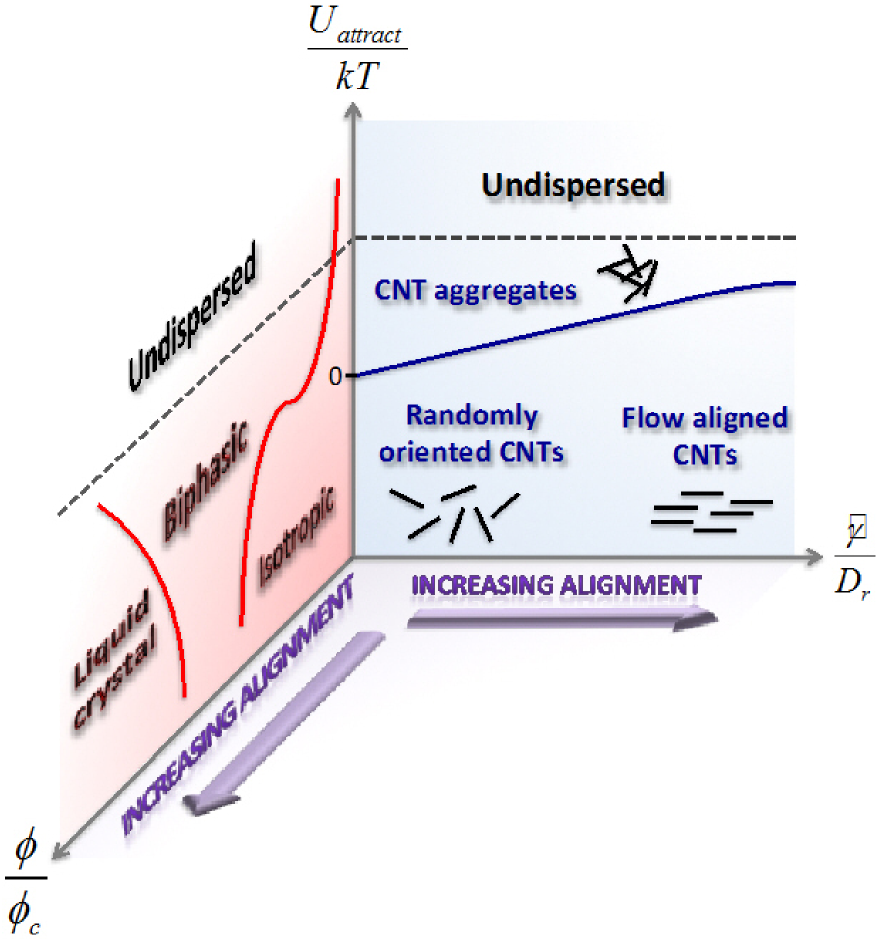

FIGURE 5.18
Typical flow behavior of suspensions containing CNTs with varying interaction potential when subjected to different strengths of shear flow ($\frac{U_{attract}}{kT}$: attraction potential normalized with Brownian energy; $\dot{\gamma}$: shear rate, D_r : rotary diffusivity). The interaction potential between CNTs can be modified through the choice of solvent and functionalization technique. The phase behavior, similar to that shown in Fig. 5.8, is given as another dimension of this parameter space (ϕ : CNT concentration; ϕ_c : critical concentration). The general observation is that CNTs that are weakly attractive tend to aggregate at low shear rates, while high shear rates tend to break up the aggregates and subsequently lead to the flow alignment of CNTs. Alternatively, intrinsic alignment of CNT can be achieved as a result of the formation of a liquid crystalline phase

Apparently, as the nanotubes are translated and rotated in a velocity gradient field, they collide with each other and interlock to form aggregates at sufficiently low shear stress. Similar phenomena have been experimentally observed for classical fibers, and particle-level simulations suggest that frictional forces alone between fiber contacts can lead to flocculation, even in the absence of attractive force.[132] Whether CNTs aggregate in flow and, if they do, the type of aggregate formed depends on the flow conditions as well as the interaction potential, which can be modified through the choice of solvent and functionalization[130]. The type of aggregate structures that can form under shear is very rich. Hobbie and co-workers[39] mapped out a “phase diagram” for CNT-PIB suspensions as a function of concentration, gap size, and shear rate (stress), suggesting that the aggregate state can be classified as “cavitated networks”, “vorticity bands”, “isolated aggregates”, and “flowing nematics”.

Aggregates can be isotropic or anisotropic, where in the latter case they align with the flow or vorticity direction (perpendicular to both the flow and velocity gradient directions)[59, 130]. An intriguing example of vorticity-aligned CNT aggregates has been independentlyreported by Hobbie et al.[39, 109] and Ma et al.[89] and referred to as “vorticity bands” and “helical bands”, respectively. This type of structure tends to form under low shear (stress) conditions and small confinement, and their formation is conjectured to be a result of mechanical aggregation, confinement, and the rotational flow component inherent to simple shear. Figure 5.19 shows a series of optical snapshots that capture the formation of such structures in a simple shear flow. This type of structure has been associated with a negative first normal stress difference and a transient increase and subsequent decrease in viscosity,[109] while in another study no significant change in the (transient) shear viscosity was observed during the formation of such structures[89]. As shear rate increases, the general observation is that the size of the aggregates decreases[57], whilst the degree of CNT alignment along the flow direction increases[28, 114, 133] as shown in Fig. 5.18.

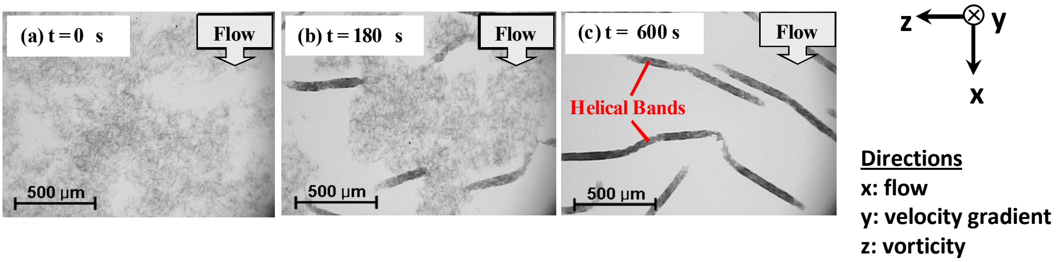

FIGURE 5.19

Time evolution of optical microstructure as low shear ($0.5\ s^{-1}$) was applied to 0.03% (as-produced) MWNTs suspended in a low-viscosity epoxy (UV 60-7155, Epoxies Inc.) confined within a gap of 130 μm. Helical Band (HB) structures were identified as shown in figure (c). Temperature = 25°C.[59, 89]

Microstructure-based Rheological Modeling

Steady shear thinning data, as described in section 3.1, can be fitted with a number of empirical equations, such as the Cross model,[28, 58] the Carreau model,[40, 134] the Krieger-Dougherty model,[34, 135] the Bingham model,[41, 55] and the Herschel-Bulkley model.[41, 136] In contrast, there are only a few studies[56, 57, 137, 138] focusing on detailed modeling of the rheology of CNT suspensions. Given their shape and relatively large persistence length, modeling CNTs as rigid rods provides a good starting point. For rod suspensions, a constitutive equation that relates the stress to the microstructure (or more specifically the orientation distribution of rods) is given as:[66, 139, 140]

$$\tau = -PI + 2\eta_s D + \tau^f \tag{7}$$

where *P* denotes the pressure, I is the identity matrix, η_s is the matrix viscosity, and D is the strain rate tensor (symmetric component of the velocity gradient tensor). τ^f is the stress tensor contribution due to the presence of rods and is given as[55]:

$$\begin{aligned} \tau^f &= 2\eta N_p \left(\mathbf{a}_4 : \mathbf{D}\right) + \beta \boldsymbol{D}_r \left(\mathbf{a}_2 - \frac{\mathbf{I}}{3}\right) \\ \mathrm{a}_4 &= \int_{S(0,1)} \left(\rho \otimes \rho \otimes \rho \otimes \rho\right) \psi\left(\rho, \mathrm{x}, t\right) d\rho \\ \mathrm{a}_2 &= \int_{S(0,1)} \left(\rho \otimes \rho\right) \psi\left(\rho, \mathrm{x}, t\right) d\rho \end{aligned} \tag{8}$$

where *Np* is a scalar parameter that depends on the rod concentration as well as the aspect ratio of rods;**a**$_4$ and **a**$_2$are the fourth-order and second order orientation tensors respectively; **ρ** is an unit vector aligned in the rod axis direction; *S*(0,1) represents the surface of the unit sphere where the rod orientation is defined; and ψ(**ρ**, x, *t*)represents the probability of having a CNT aligning in direction **ρ** , for physical coordinates x and time t. For dilute rod suspensions, $\beta = 6\nu\xi$, where ν is the number concentration of rods and ξ is the viscous drag coefficient.[55, 56]The shear stress is a function of the orientation distribution of rods ψcan be calculated by solving the Fokker-Planck (FP) equation, which is also known as the *Smoluchowski* equation in the context of rod suspension modeling[55, 141].

$$\frac{D\psi}{Dt} + \frac{\partial}{\partial \rho} \cdot \left(\frac{d\rho}{dt}\psi\right) = \frac{\partial}{\partial \rho} \cdot \left(D_r \frac{\partial \psi}{\partial \rho}\right) \tag{9}$$

Eqn 9 considers a competition between the hydrodynamic force that aligns rods with the flow direction and events that randomize the rod/CNT orientation. The second term on the left hand side of eqn 9 is an advection term and the term *d***ρ**/*dt* is given by the Jeffery equation[55, 142]:

$$\frac{d\rho}{dt} = \Omega \cdot \rho + k\mathrm{D} \cdot \rho - k(\mathrm{D} : (\rho \otimes \rho))\rho \tag{10}$$

where Ω is the vorticity tensor, *k* is a shape factor and is given as: $k = \left(\lambda^2 - 1\right) / \left(\lambda^2 + 1\right)$with *λ* as the (effective) aspect ratio. For cylindrical rods, $\lambda = 0.7a$ where *a* is the actual aspect ratio (length to diameter ratio) of the cylinder[143]. For the high aspect ratios appropriate for CNTs (*a*> 100), *k*≈ 1.

In eqn 9, a key parameter is the rotary diffusion coefficient (D_r), which represents the rate at which the rods randomize their orientation. For dilute suspensions, Brownian motion is considered to be the source of randomization, whereas in the case of semi-dilute suspensions, “caging” effects[54] and rod-rod interactions[144] can also play an important role.[55] Ma and co-workers[56] used this model (eqns 7-10) to describe the rheology of non-aggregating CNT suspensions, where the CNTs were functionalized and suspended within a Newtonian epoxy matrix. Reasonable agreement between experimental data and the model was obtained by using N_p and D_r as the fitting parameters. The success of the model suggests that the shear thinning effect experimentally observed in non-aggregating CNT suspensions is probably a result of progressive alignment of CNT in the flow direction as the shear rate increases. From the simulation results of orientation distribution function, a scalar order parameter (S) can be calculated using the following equation[55]:

$$S = \sqrt{\frac{3}{2}(\mathbf{Q}:\mathbf{Q})} \tag{11}$$

where $\mathbf{Q} = \left(\mathbf{a}_2 - \frac{\mathbf{I}}{3}\right)$, **I** is the identity matrix and $\mathbf{a_2}$ is the second order orientation tensor (as defined in eqn 8). As before, S provides a quantitative measure of the degree of alignment with $S = 0$ representing an isotropic orientation and $S = 1$ representing complete alignment. As shown in Fig. 5.20, this model predicts a high degree of orientation ($S = 0.92$), as the suspension viscosity approaches the viscosity of the suspending medium. Such high degree of orientation has yet to be confirmed experimentally. The authors also reported experimental LVE data, but the modeling was found to be more challenging and requires the use of a phenomenological relation of which the exact physical origin still remains unclear.[56]

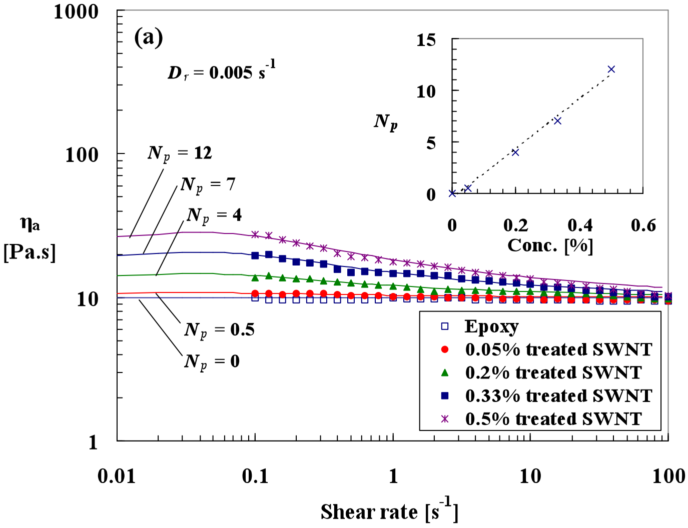

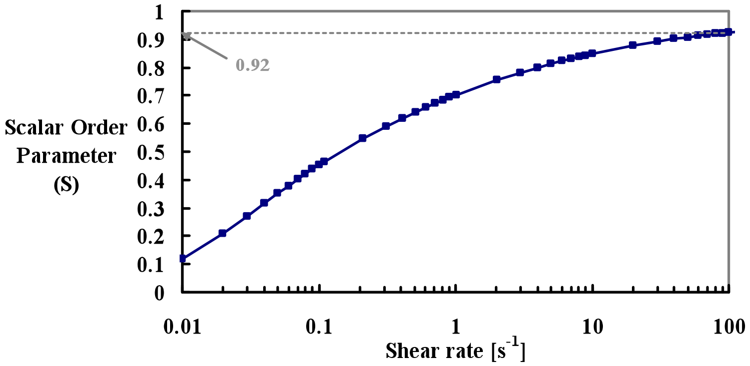

FIGURE 5.20
(a) Shear viscosity (η_a) as a function of shear rate for different concentrations of treated (functionalized) SWNTs. Orientation model fittings are represented by solid line. N_p and D_r are the fitting parameters. (b) Scalar order parameter (S) as a function of shear rate, where $0 \leq S \leq 1$. Reproduced from [56]

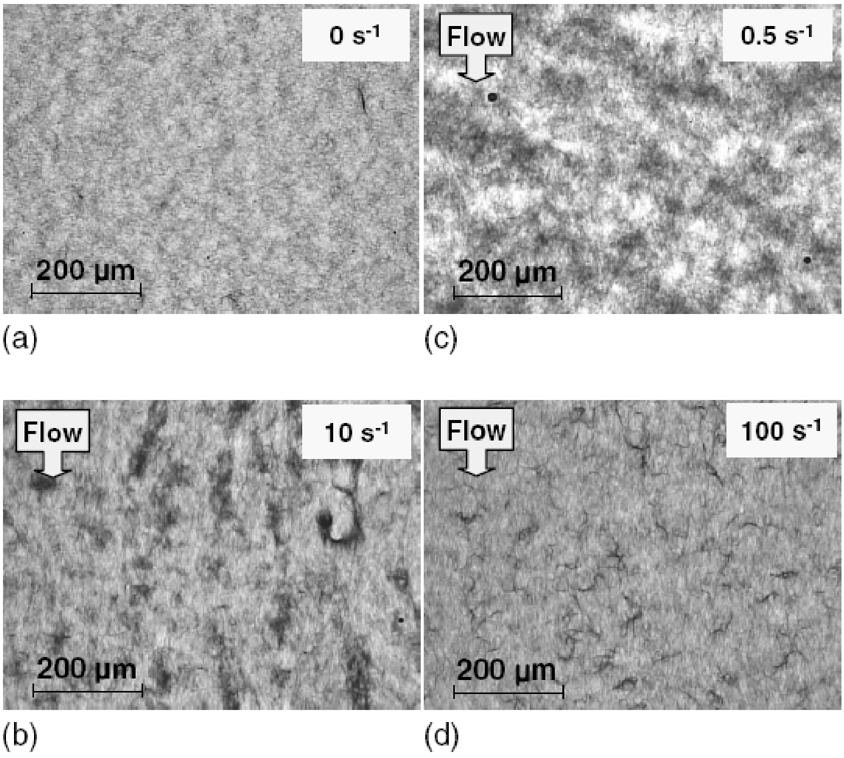

FIGURE 5.21
Optical microstructure of 0.1% CNT suspended in an epoxy resin (without hardener) after shearing at (a) 0 s^{-1}, (b) 0.5 s^{-1}, (c) 10 s^{-1} and (d) 100 s^{-1}. The micrographs were captured after a shearing time of 100 s and using the Cambridge Shear System (CSS 450) with an optical depth of 130 µm. Adapted from [57]

In the case of CNT suspensions where there is clear optical evidence of aggregation (Fig. 5.21), the shear-thinning behavior tended to be more pronounced[28] and the experimental results cannot be explained by a FP based orientation model[57]. Inspired by earlier work on associative polymer modeling[145, 146], Ma et al.[57] formulated a new model called the "aggregation/orientation (AO) model". In this model, the authors considered that CNTs exist in different entanglement states and have different tendencies to align in the shear flow (i.e $D_r = D_r(n)$). The entanglement state of a CNT is denoted by a population number $n \in [0,1]$, with *n* = 0 representing a CNT free from entanglement and *n* = 1 representing a CNT at the highest possible entanglement state. The Fokker-Planck equation was modified as:

$$\frac{\partial\psi(t,\rho,n)}{\partial t}=\frac{\partial\psi(t,\rho,n)}{\partial t}\bigg|_{Orientation}+\frac{\partial\psi(t,\rho,n)}{\partial t}\bigg|_{Aggregation}$$
$$=\left\{-\frac{\partial}{\partial\rho}\left\{\psi(t,\rho,n)\frac{\partial\rho}{\partial t}\right\}+\frac{\partial}{\partial\rho}\left\{D_r(n)\frac{\partial\psi(t,\rho,n)}{\partial t}\right\}\right\}$$
$$+\left\{v_c\int_{r=0}^{r=n}\psi(t,\rho,r)dr+v_d\int_{r=n}^{r=1}\psi(t,\rho,r)dr-v_d\psi(t,\rho,n)\int_{r=0}^{r=n}dr-v_c\psi(t,\rho,n)\int_{r=n}^{r=1}dr\right\} \quad (12)$$

where v_c is the rate of aggregation and v_d is the rate of disaggregation. A detailed mathematical derivation is given elsewhere[57]. For homogenous flow at steady state, eqn 12 reduces to:

$$\left\{-\frac{\partial}{\partial\rho}\left\{\psi(\rho,n)\frac{d\rho}{dt}\right\}+\frac{\partial}{\partial\rho}\left\{D_r(n)\frac{\partial\psi(\rho,n)}{\partial\rho}\right\}\right\}+$$
$$+\left\{v_c\int_{r=0}^{r=n}\psi(\rho,r)dr+v_d\int_{r=n}^{r=1}\psi(\rho,r)dr-v_d\psi(\rho,n)\int_{r=0}^{r=n}dr-v_c\psi(\rho,n)\int_{r=n}^{r=1}dr\right\}=0 \quad (13)$$

A number of assumptions have been made to reduce the number of model parameters. By introducing one additional parameter ($\alpha = v_d / v_c$) to describe the aggregation/ disaggregation kinetics, the AO model was able to capture the more pronounced shear thinning observed in aggregating CNT suspensions[57] (Fig. 5.22a).

In the literature, similar approaches[137, 138] have been used to model (aggregating) CNT suspensions, by considering CNTs as finitely extensible non-linear elastic (FENE) dumbbells, instead of inextensible rigid rods. These models successfully capture the shear-thinning behavior but fail to capture the LVE results. It is worth noting that unlike the original associative polymer model[145] and similar models[137, 138], the AO model considers more than two discrete populations to reflect the complexity of aggregate structures observed experimentally (Fig. 5.21). Besides that, the assumption about the diffusivity of "free" and "highly entangled" populations is different. In ref [57], CNTs that are free from entanglement (*n = 0*) were assumed to have a diffusivity of zero (i.e.$D_r|_{n=0} = 0$ and $D_r|_{n=0} < D_r|_{n=1}$), whereas in ref [145] entangled CNTs (*n = 1*) were assumed to have a diffusivity of zero (i.e.$D_r|_{n=1} = 0$ and $D_r|_{n=1} < D_r|_{n=0}$). The assumption used in ref [57] is supported by experimental observations that highly entangled CNTs in the form of aggregates tend to rotate during a simple shear flow [89, 147]; however, the authors also note that the quality of the fitting is not affected if the opposite is assumed to be true [148].

By fitting the AO model to experimental data, the population distribution was simulated for various shear flow conditions and CNT concentrations. As shown in Figs. 5.22b and 5.22c, the population distribution skews towards *n* = 1 (entangled CNT) at a low shear rate of 1 s^{-1} but skews towards *n* = 0 (non-entangled CNT) at a higher shear rate of 10 s^{-1}. The simulation results are consistent with experimental observations that low shear induces aggregation and at higher shear rates CNTs become less entangled. Moreover, the simulation results (Fig. 5.22b) also suggested that CNT suspensions at higher concentration have a higher tendency to aggregate (skew more towards *n* = 1), which can possibly be explained by smaller separation between CNTs and thus a higher chance of colliding and aggregating at high concentrations.

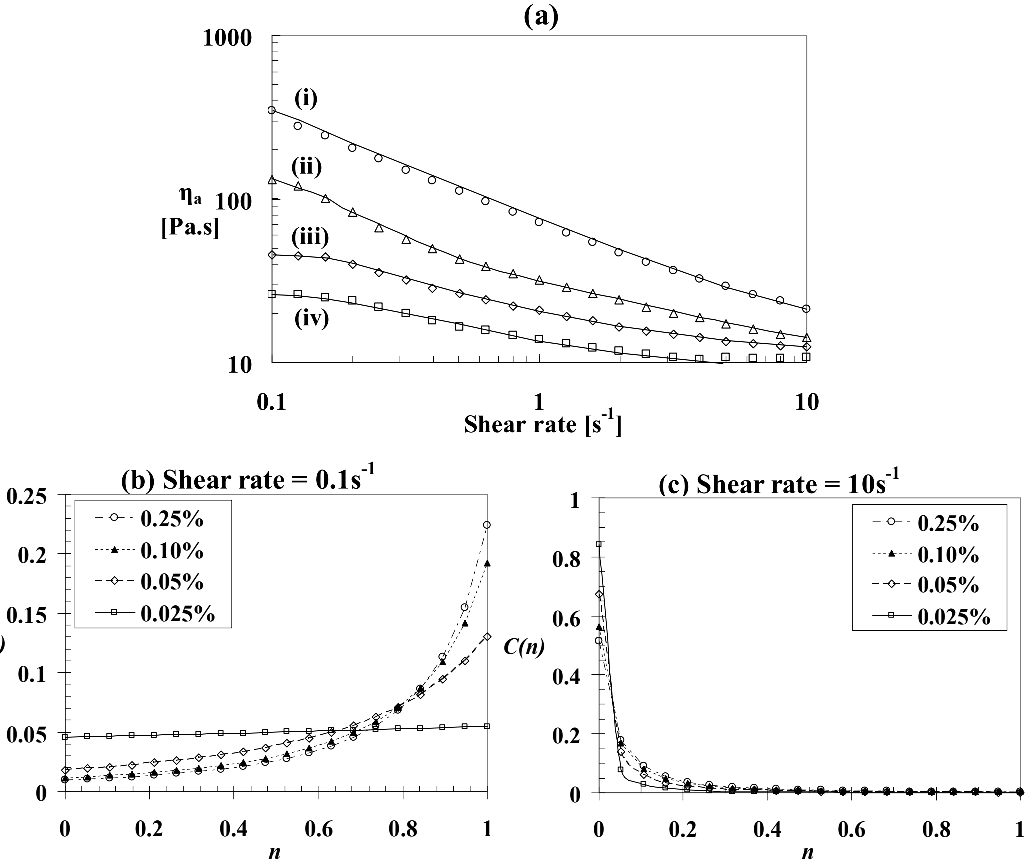

FIGURE 5.22

(a) Aggregation/orientation (AO) model fitting to experimental η_a data at different CNT concentration levels: (i) 0.25%, (ii) 0.1%, (iii) 0.05% and (iv) 0.025%. Experimental data are represented by unfilled symbols and the lines are the best fits using the AO model. (b) and (c) shows the population distribution *C(n)* at two different shear rates. At a low shear rate of 1 s^{-1} (Fig. b), *C(n)* skews towards *n* = 1 (entangled CNT), whereas at a higher shear rate of 10 s^{-1}, *C(n)* skews towards *n* = 0 (non-entangled CNT). Fig. (b) also shows that CNT tended to aggregate (population distribution skews towards *n* = 1) at higher CNT concentration. Adapted from [57]

Conclusion

CNT suspensions represent a relatively novel and complex class of suspension system of which some basic understanding has been established over the last decade. In this review paper, we first reviewed our current understanding of CNTs as individual entities suspended within a liquid medium. Recent fluorescence microscopy studies[53] showed that the persistence length of CNTs scales with the cube of the CNT diameter, in agreement with the elastic continuum model prediction. The persistence length of SWNTs was identified experimentally to be in the range of 26 to 138 µm, larger than many polymer molecules used in commercial fibers with high mechanical strength. Having established the bending dynamics of individual CNTs, we then discussed a wide range of CNT suspensions, from a disordered isotropic liquid state to an ordered liquid crystalline state with high degree of local orientation. A number of experimental techniques have been used to probe the microstructure of CNT suspensions during flow, providing important insight into the underlying physics. For dilute and semi-dilute suspensions, shear flow is able to align CNTs in the flow direction and modeling CNTs as rigid rods that progressively align in flow appears to work reasonably well in explaining the relatively mild shear thinning behavior of non-aggregating CNT suspensions[56]. In contrast, aggregating CNT suspensions show very complex microstructural evolution in flow, coupled with a more pronounced shear-thinning behavior. Such behavior cannot be described by a relatively simple orientation model, but was successfully described using an aggregation/orientation model[57] which considers a hierarchy of CNT aggregate structures in flow and alternatively by including the effect of CNT-CNT interactions.[152] According to LVE studies, CNTs form a physical network as the concentration goes above certain critical or percolation threshold value. The network can be destroyed at large strains and the type of network formation depend largely on the length of the CNTs. Scaling analysis on surfactant-stabilized CNT suspensions suggests that the elasticity of the suspension is coming from the interaction between CNTs instead of bending and stretching of CNTs. However, a consensus has not yet been reached concerning the exact origin of network elasticity. In addition to CNT interactions, CNT bending and stretching have been proposed as possible origins for elasticity. In terms of extensional rheology, as CNT suspensions undergo uniaxial elongation, the mode of liquid filament breakup depends on the type of microstructure present in the system. Suspensions of CNT aggregates tend to form non-uniform liquid filaments that break up prematurely, whereas non-aggregating CNT suspensions tend to form more uniform and stable filaments.

At very high concentrations, CNTs can form liquid crystalline phases, showing optical features and rheological signatures similar to those observed in the case of liquid crystalline polymers. Phase diagrams have been successfully constructed for various CNT liquid crystalline systems and in all reported cases a biphasic regime is observed where an isotropic phase co-exists with an ordered liquid crystalline phase. However, the experimental biphasic regime is much broader than that predicted by classical theories. Several authors attributed this to the (length) polydispersity of CNTs, which was substantiated by later modeling efforts. In addition to length, diameter and flexibility of also play an important role in affecting the type of liquid crystalline texture formation.

To summarize, CNT suspensions closely resemble classical rigid rod and liquid crystalline polymer systems in many ways. Modeling these complex fluids as such provides a good starting point for understanding this new type of fibrous material. However, there are still scientific questions yet to be answered and research areas deserving further investigation. For instance, orientation models have predicted a high degree of CNT alignment in both shear and extensional flows, but this has yet to be confirmed experimentally. In the case of CNT liquid crystalline solutions, understanding the evolution of liquid crystalline domains is important for identifying flow conditions that will maximize the degree of alignment during processing and may provide additional insights into the origin of the negative first normal stress difference. In the literature, there is also a wealth of experimental data on systems with a viscoelastic suspending medium yet to be modeled[153]The behavior of CNTs adsorbed at a fluid-fluid interface is relevant to stabilizing emulsions and foams,[154,155] but the corresponding interfacial rheology remains largely unexplored. Finally, given all these unresolved questions, we believe rheological studies on CNT suspensions with an ultimate goal of elucidating the structure-rheology relationships will remain an active area of research.

Acknowledgements

The authors would like to acknowledge Prof. Erik K. Hobbie, North Dakota State University, for his intellectual inputs on the early draft of this book chapter. This material is based upon work supported by the U.S. National Science Foundation CAREER award under grant no. 1253613.

References

1. Z. C. Tu and Z. Ou-Yang, Physical Review B **65** (23), 233407 (2002).
2. D. A. Walters, L. M. Ericson, M. J. Casavant, J. Liu, D. T. Colbert, K. A. Smith and R. E. Smalley, Applied Physics Letters **74** (25), 3803-3805 (1999).
3. J. Hone, M. Whitney and A. Zettl, Synthetic Metals **103** (1-3), 2498-2499 (1999).
4. A. Thess, R. Lee, P. Nikolaev, H. J. Dai, P. Petit, J. Robert, C. H. Xu, Y. H. Lee, S. G. Kim, A. G. Rinzler, D. T. Colbert, G. E. Scuseria, D. Tomanek, J. E. Fischer and R. E. Smalley, Science **273** (5274), 483-487 (1996).
5. R. E. Smalley, MRS Bulletin **30** (6), 412-417 (2005).
6. C. Dekker, Physics Today **52** (5), 22-28 (1999).
7. W. A. de Heer, MRS Bulletin **29** (4), 281-285 (2004).
8. P. Calvert, Nature **399** (6733), 210-211 (1999).
9. S. Saito, Science **278** (5335), 77-78 (1997).
10. M. J. Green, N. Behabtu, M. Pasquali and W. W. Adams, Polymer **50** (21), 4979-4997 (2009).
11. M. S. P. Shaffer and A. H. Windle, Macromolecules **32** (20), 6864-6866 (1999).
12. C. L. Pint, S. T. Pheasant, M. Pasquali, K. E. Coulter, H. K. Schmidt and R. H. Hauge, Nano Letters **8** (7), 1879-1883 (2008).
13. X. S. Li, X. F. Zhang, L. J. Ci, R. Shah, C. Wolfe, S. Kar, S. Talapatra and P. M. Ajayan, Nanotechnology **19** (45), 455609-455601-455607 (2008).
14. Y. L. Li, L. H. Zhang, X. H. Zhong and A. H. Windle, Nanotechnology **18** (22), 225604-225601-225606 (2007).
15. Y. L. Li, I. A. Kinloch and A. H. Windle, Science **304** (5668), 276-278 (2004).
16. P. Nikolaev, M. J. Bronikowski, R. K. Bradley, F. Rohmund, D. T. Colbert, K. A. Smith and R. E. Smalley, Chemical Physics Letters **313** (1-2), 91-97 (1999).
17. A. R. Harutyunyan, G. Chen, T. M. Paronyan, E. M. Pigos, O. A. Kuznetsov, K. Hewaparakrama, S. M. Kim, D. Zakharov, E. A. Stach and G. U. Sumanasekera, Science **326** (5949), 116-120 (2009).

18. R. E. Smalley, Y. Li, V. C. Moore, B. K. Price, R. Colorado, H. K. Schmidt, R. H. Hauge, A. R. Barron and J. M. Tour, Journal of the American Chemical Society **128** (49), 15824-15829 (2006).
19. Y. H. Wang, M. J. Kim, H. W. Shan, C. Kittrell, H. Fan, L. M. Ericson, W. F. Hwang, S. Arepalli, R. H. Hauge and R. E. Smalley, Nano Letters **5** (6), 997-1002 (2005).
20. S. M. Bachilo, L. Balzano, J. E. Herrera, F. Pompeo, D. E. Resasco and R. B. Weisman, Journal of the American Chemical Society **125** (37), 11186-11187 (2003).
21. Y. M. Li, D. Mann, M. Rolandi, W. Kim, A. Ural, S. Hung, A. Javey, J. Cao, D. W. Wang, E. Yenilmez, Q. Wang, J. F. Gibbons, Y. Nishi and H. J. Dai, Nano Letters **4** (2), 317-321 (2004).
22. L. T. Qu, F. Du and L. M. Dai, Nano Letters **8** (9), 2682-2687 (2008).
23. A. G. Rinzler, Nature Nanotechnology **1** (1), 17-18 (2006).
24. M. S. Arnold, A. A. Green, J. F. Hulvat, S. I. Stupp and M. C. Hersam, Nature Nanotechnology **1** (1), 60-65 (2006).
25. M. S. Strano, C. A. Dyke, M. L. Usrey, P. W. Barone, M. J. Allen, H. Shan, C. Kittrell, R. H. Hauge, J. M. Tour and R. E. Smalley, Science **301** (5639), 1519-1522 (2003).
26. R. Krupke, F. Hennrich, H. v. Lohneysen and M. M. Kappes, Science **301** (5631), 344-347 (2003).
27. A. W. K. Ma, K. M. Yearsley, F. Chinesta and M. R. Mackley, Proc. IMechE, Part N: J. Nanoengineering and Nanosystems **222**, 71-94 (2009).
28. S. S. Rahatekar, K. K. K. Koziol, S. A. Butler, J. A. Elliott, M. S. P. Shaffer, M. R. Mackley and A. H. Windle, Journal of Rheology **50** (5), 599-610 (2006).
29. Y. S. Song and J. R. Youn, Carbon **43** (7), 1378-1385 (2005).
30. V. A. Davis, L. M. Ericson, A. N. G. Parra-Vasquez, H. Fan, Y. H. Wang, V. Prieto, J. A. Longoria, S. Ramesh, R. K. Saini, C. Kittrell, W. E. Billups, W. W. Adams, R. H. Hauge, R. E. Smalley and M. Pasquali, Macromolecules **37** (1), 154-160 (2004).
31. F. Du, R. C. Scogna, W. Zhou, S. Brand, J. E. Fischer and K. I. Winey, Macromolecules **37** (24), 9048-9055 (2004).
32. C. A. Mitchell, J. L. Bahr, S. Arepalli, J. M. Tour and R. Krishnamoorti, Macromolecules **35** (23), 8825-8830 (2002).
33. L. A. Hough, M. F. Islam, P. A. Janmey and A. G. Yodh, Physical Review Letters **93** (16), 168102 (2004).
34. B. Kim, H. Park and W. M. Sigmund, Colloids and Surfaces a-Physicochemical and Engineering Aspects **256** (2-3), 123-127 (2005).
35. B. Schartel, P. Potschke, U. Knoll and M. Abdel-Goad, European Polymer Journal **41** (5), 1061-1070 (2005).
36. P. Potschke, T. D. Fornes and D. R. Paul, Polymer **43** (11), 3247-3255 (2002).
37. Y. Y. Huang, S. V. Ahir and E. M. Terentjev, Physical Review B **73** (12), - (2006).
38. T. McNally, P. Potschke, P. Halley, M. Murphy, D. Martin, S. E. J. Bell, G. P. Brennan, D. Bein, P. Lemoine and J. P. Quinn, Polymer **46** (19), 8222-8232 (2005).
39. E. K. Hobbie and D. J. Fry, Physical Review Letters **97** (3), - (2006).
40. S. B. Kharchenko, J. F. Douglas, J. Obrzut, E. A. Grulke and K. B. Migler, Nature Materials **3** (8), 564-568 (2004).
41. I. A. Kinloch, S. A. Roberts and A. H. Windle, Polymer **43** (26), 7483-7491 (2002).
42. B. Safadi, R. Andrews and E. A. Grulke, Journal of Applied Polymer Science **84** (14), 2660-2669 (2002).
43. J. L. Bahr and J. M. Tour, Journal of Materials Chemistry **12** (7), 1952-1958 (2002).
44. C. A. Dyke and J. M. Tour, Journal of Physical Chemistry A **108** (51), 11151-11159 (2004).

45. D. A. Britz and A. N. Khlobystov, Chemical Society Reviews **35** (7), 637-659 (2006).
46. S. Banerjee, T. Hemraj-Benny and S. S. Wong, Advanced Materials **17** (1), 17-29 (2005).
47. M. J. Green, A. N. G. Parra-Vasquez, N. Behabtu and M. Pasquali, J Chem Phys **131** (8), 084901 (2009).
48. S. Ramesh, L. M. Ericson, V. A. Davis, R. K. Saini, C. Kittrell, M. Pasquali, W. E. Billups, W. W. Adams, R. H. Hauge and R. E. Smalley, Journal of Physical Chemistry B **108** (26), 8794-8798 (2004).
49. L. M. Ericson, H. Fan, H. Q. Peng, V. A. Davis, W. Zhou, J. Sulpizio, Y. H. Wang, R. Booker, J. Vavro, C. Guthy, A. N. G. Parra-Vasquez, M. J. Kim, S. Ramesh, R. K. Saini, C. Kittrell, G. Lavin, H. Schmidt, W. W. Adams, W. E. Billups, M. Pasquali, W. F. Hwang, R. H. Hauge, J. E. Fischer and R. E. Smalley, Science **305** (5689), 1447-1450 (2004).
50. N. Behabtu, M. J. Green and M. Pasquali, Nano Today **3** (5-6), 24-34 (2008).
51. C. A. Martin, J. K. W. Sandler, M. S. P. Shaffer, M. K. Schwarz, W. Bauhofer, K. Schulte and A. H. Windle, 2004 (unpublished).
52. P. M. Ajayan, O. Stephan, C. Colliex and D. Trauth, Science **265** (5176), 1212-1214 (1994).
53. N. Fakhri, D. A. Tsyboulski, L. Cognet, R. B. Weisman and M. Pasquali, Proceedings of the National Academy of Sciences **106** (34), 14219-14223 (2009).
54. M. Doi and S. S. Edwards, *The theory of polymer dynamics*. (Clarendon, 1986).
55. R. G. Larson, *The structure and rheology of complex fluids*. (Oxford University Press, New York ; Oxford, 1999).
56. A. W. K. Ma, F. Chinesta and M. R. Mackley, J Rheol **53** (3), 547-573 (2009).
57. W. K. A. Ma, F. Chinesta, A. Ammar and M. R. Mackley, J Rheol **52** (6), 1311-1330 (2008).
58. M. M. Cross, Journal of Colloid Science **20** (5), 417-& (1965).
59. A. W. K. Ma, PhD dissertation, University of Cambridge, 2009.
60. S. Lin-Gibson, J. A. Pathak, E. A. Grulke, H. Wang and E. K. Hobbie, Physical Review Letters **92** (4) (2004).
61. S. G. Mason, Pulp Paper Mag. Can. **49**, 99-104 (1948).
62. S. G. Mason, Tappi J. **33**, 440-444 (1950).
63. B. Dan, G. C. Irvin and M. Pasquali, Acs Nano **3** (4), 835-843 (2009).
64. A. N. G. Parra-Vasquez, I. Stepanek, V. A. Davis, V. C. Moore, E. H. Haroz, J. Shaver, R. H. Hauge, R. E. Smalley and M. Pasquali, Macromolecules **40** (11), 4043-4047 (2007).
65. J. G. Kirkwood and P. L. Auer, The Journal of Chemical Physics **19** (3), 281-283 (1951).
66. Batchelo.Gk, Journal of Fluid Mechanics **41**, 545-& (1970).
67. S. S. Rahatekar, K. K. Koziol, S. R. Kline, E. K. Hobbie, J. W. Gilman and A. H. Windle, Advanced Materials **21** (8), 874-878 (2009).
68. Z. H. Fan and S. G. Advani, Journal of Rheology **51** (4), 585-604 (2007).
69. J. G. Kirkwood and R. J. Plock, The Journal of Chemical Physics **24** (4), 665-669 (1956).
70. C. W. Macosko, *Rheology : principles, measurements, and applications*. (VCH, New York, NY ; Cambridge, 1994).
71. D. W. Litchfield and D. G. Baird, in *Rheology Reviews*, edited by D. M. Binding and K. Walters (The British Society of Rheology, 2006).
72. M. Abdel-Goad and P. Potschke, Journal of Non-Newtonian Fluid Mechanics **128** (1), 2-6 (2005).
73. Y. Y. Huang, S. V. Ahir and E. M. Terentjev, Physical Review B**73** (12), 125422 (2008).
74. V. Trappe and D. A. Weitz, Physical Review Letters **85** (2), 449-452 (2000).
75. E. K. Hobbie and D. J. Fry, Journal of Chemical Physics **126** (12) (2007).

76. K. Kordas, T. Mustonen, G. Toth, H. Jantunen, M. Lajunen, C. Soldano, S. Talapatra, S. Kar, R. Vajtai and P. M. Ajayan, Small **2** (8-9), 1021-1025 (2006).
77. J. Jader, N. Willenbacher, G. Engstrom and L. Jarnstrom, Journal of Pulp and Paper Science **31** (4), 181-187 (2005).
78. A. W. K. Ma, F. Chinesta, T. Tuladhar and M. R. Mackley, Rheol. Acta **47** (4), 447-457 (2008).
79. M. K. Tiwari, A. V. Bazilevsky, A. L. Yarin and C. M. Megaridis, Rheologica Acta **48** (6), 597-609 (2009).
80. A. V. Bazilevsky, V. M. Entov and A. N. Rozhkov, in *Third European Rheology Conference*, edited by D. R. Oliver (Elsevier, New York, 1990).
81. J. E. Matta and R. P. Tytus, Journal of Non-Newtonian Fluid Mechanics **35** (2-3), 215-229 (1990).
82. G. H. McKinley and T. Sridhar, Annual Review of Fluid Mechanics **34**, 375-415 (2002).
83. R. F. Liang and M. R. Mackley, Journal of Non-Newtonian Fluid Mechanics **52** (3), 387-405 (1994).
84. S. L. Anna, G. H. McKinley, D. A. Nguyen, T. Sridhar, S. J. Muller, J. Huang and D. F. James, 2001 (unpublished).
85. G. H. McKinley and A. Tripathi, Journal of Rheology **44** (3), 653-670 (2000).
86. D. T. Papageorgiou, Physics of Fluids **7** (7), 1529-1544 (1995).
87. Batchelo.Gk, Journal of Fluid Mechanics **46** (APR27), 813-& (1971).
88. G. B. Weinberger and J. D. Goddard, Int. J. Multiphase Flow **1**, 465-486 (1974).
89. A. W. K. Ma, M. R. Mackley and S. S. Rahatekar, Rheologica Acta **46** (7), 979-987 (2007).
90. J. A. N. Zasadzinski and R. B. Meyer, Physical Review Letters **56** (6), 636-638 (1986).
91. C. Zakri and P. Poulin, Journal of Materials Chemistry **16** (42), 4095-4098 (2006).
92. C. Zakri, Liquid Crystals Today **16** (1), 1 - 11 (2007).
93. P. K. Rai, R. A. Pinnick, A. N. G. Parra-Vasquez, V. A. Davis, H. K. Schmidt, R. H. Hauge, R. E. Smalley and M. Pasquali, Journal of the American Chemical Society **128** (2), 591-595 (2006).
94. W. Zhou, P. A. Heiney, H. Fan, R. E. Smalley and J. E. Fischer, Journal of the American Chemical Society **127** (6), 1640-1641 (2005).
95. A. W.K. Ma, J. Nam, N. Behabtu, F. Mirri, C. C. Young, B. Dan, D. Tsentalovich, M. Majumder, L. Song, Y. Cohen, P. M. Ajayan and M. Pasquali, Ind. Eng. Chem. Res., **52**, 8705 - 8713 (2013).
96. A. Saha, S. Ghosh, R. B. Weisman and A. A. Marti, ACS Nano, **6**, 9737 – 9744 (2012).
97. B. Dan, A. W. K. Ma, E. H. Haroz, J. Kono and M. Pasquali, Ind. Eng. Chem. Res. **51**, 10232 – 10237 (2012).
98. N. Behabtu, C. C. Young, D. E. Tsentalovich, O. Kleinerman, X. Wang, A. W. K. Ma, E. A. Bengio, R. F. Waarbeek, J. J. Jong, R. E. Hoogerwerf, S. B. Fairchild, J. B. Ferguson, B. Maruyama, J. Kono, Y. Talmon, Y. Cohen, M. J. Otto and M. Pasquali, Science, **339**, 182 – 186 (2013).
99. V. A. Davis, PhD dissertation, Rice University, 2006.
100. L. Onsager, Annals of the New York Academy of Sciences **51** (4), 627-659 (1949).
101. P. J. Flory, Proceedings of the Royal Society of London Series a-Mathematical and Physical Sciences **234** (1196), 73-89 (1956).
102. H. H. Wensink and G. J. Vroege, Journal of Chemical Physics **119** (13), 6868-6882 (2003).
103. W. H. Song, I. A. Kinloch and A. H. Windle, Science **302** (5649), 1363-1363 (2003).
104. W. H. Song and A. H. Windle, Macromolecules **38** (14), 6181-6188 (2005).

105. W. H. Song and A. H. Windle, Advanced Materials **20** (16), 3149-3154 (2008).
106. A. M. Donald, A. H. Windle and S. Hanna, *Liquid crystalline polymers*, Cambridge University Press, 2006.
107. S. E. Moulton, M. Maugey, P. Poulin and G. G. Wallace, Journal of the American Chemical Society **129** (30), 9452-9457 (2007).
108. S. Badaire, C. Zakri, M. Maugey, A. Derre, J. N. Barisci, G. Wallace and P. Poulin, Advanced Materials **17** (13), 1673-+ (2005).
109. S. Badaire, P. Poulin, M. Maugey and C. Zakri, Langmuir **20** (24), 10367-10370 (2004).
110. M. F. Islam, A. M. Alsayed, Z. Dogic, J. Zhang, T. C. Lubensky and A. G. Yodh, Physical Review Letters **92** (8) (2004).
111. J. Mewis, 1996 (unpublished).
112. G. Marrucci, in *Liquid Crystallinity in Polymers: Principles and Fundamental Properties*, edited by A. Ciferri (VCH Publishers, New York, 1991).
113. M. Pasquali, Nature Materials **3** (8), 509-510 (2004).
114. S. Lin-Gibson, J. A. Pathak, E. A. Grulke, H. Wang and E. K. Hobbie, Physical Review Letters **92** (4), 048302 (2004).
115. Z. P. Yang, L. J. Ci, J. A. Bur, S. Y. Lin and P. M. Ajayan, Nano Letters **8** (2), 446-451 (2008).
116. R. Duggal and M. Pasquali, Physical Review Letters **96** (24) (2006).
117. S. Onogi and T. Asada, *Rheology and Rheo-optics of Polymer Liquid Crystals*, Plenum Press, New York, (1980).
118. S. Pujari, S. S. Rahatekar, J. W. Gilman, K. K. Koziol, A. H. Windle and W. R. Burghardt, Journal of Chemical Physics **130** (21) (2009).
119. S. V. Ahir and E. M. Terentjev, Nature Materials **4** (6), 491-495 (2005).
120. W. Zhou, J. Vavro, C. Guthy, K. I. Winey, J. E. Fischer, L. M. Ericson, S. Ramesh, R. Saini, V. A. Davis, C. Kittrell, M. Pasquali, R. H. Hauge and R. E. Smalley, Journal of Applied Physics **95** (2), 649-655 (2004).
121. G. S. Duesberg, I. Loa, M. Burghard, K. Syassen and S. Roth, Physical Review Letters **85** (25), 5436-5439 (2000).
122. A. M. Rao, A. Jorio, M. A. Pimenta, M. S. S. Dantas, R. Saito, G. Dresselhaus and M. S. Dresselhaus, Physical Review Letters **84** (8), 1820-1823 (2000).
123. E. Anglaret, A. Righi, J. L. Sauvajol, P. Bernier, B. Vigolo and P. Poulin, Physical Review B **65** (16) (2002).
124. C. A. Cooper, R. J. Young and M. Halsall, 2001 (unpublished).
125. C. Zamora-Ledezma, C. Blanc, M. Maugey, C. Zakri, P. Poulin and E. Anglaret, Nano Letters **8** (12), 4103-4107 (2008).
126. M. S. Dresselhaus, G. Dresselhaus, R. Saito and A. Jorio, Physics Reports-Review Section of Physics Letters **409** (2), 47-99 (2005).
127. V. C. Moore, M. S. Strano, E. H. Haroz, R. H. Hauge, R. E. Smalley, J. Schmidt and Y. Talmon, Nano Letters **3** (10), 1379-1382 (2003).
128. A. N. G. Parra-Vasquez, N. Behabtu, M. J. Green, C. L. Pint, C. C. Young, J. Schmidt, E. Kesselman, A. Goyal, P. M. Ajayan, Y. Cohen, Y. Talmon, R. H. Hauge and M. Pasquali, Journal of the American Chemical Society (to be submitted).
129. N. Parra-Vasquez, PhD dissertation, William Marsh Rice University. Available at homer.rice.edu/~nb1, 2009.
130. A. W. K. Ma, M. R. Mackley and F. Chinesta, Int. J. Mat. Form. **1** (2), 75-81 (2008).
131. P. Potschke, A. R. Bhattacharyya and A. Janke, European Polymer Journal **40** (1), 137-148 (2004).

132. C. F. Schmid and D. J. Klingenberg, Physical Review Letters **84** (2), 290-293 (2000).
133. Z. H. Fan and S. G. Advani, Polymer **46** (14), 5232-5240 (2005).
134. P. J. Carreau, Transactions of the Society of Rheology **16** (1), 99-& (1972).
135. I. M. Krieger and T. J. Dougherty, Transactions of the Society of Rheology **3**, 137-152 (1959).
136. W. H. Herschel and R. Bulkley, Kolloid-Zeitschrift **39** (4), 291-300 (1926).
137. Y. S. Song and J. R. Youn, Korea-Australia Rheology Journal **16** (4), 201-212 (2004).
138. J. Qiu, C. Zhang, B. Wang and R. Liang, Comp. Mat. Sci. **44**, 1379-1385 (2009).
139. E. J. Hinch and L. G. Leal, Journal of Fluid Mechanics **71** (OCT14), 481-495 (1975).
140. E. J. Hinch and L. G. Leal, Journal of Fluid Mechanics **76** (JUL14), 187-208 (1976).
141. E. J. Hinch and L. G. Leal, Journal of Fluid Mechanics **52** (APR25), 683-& (1972).
142. G. B. Jeffery, Proceedings of the Royal Society of London Series a-Containing Papers of a Mathematical and Physical Character **102** (715), 161-179 (1922).
143. B. J. Trevelyan and S. G. Mason, Journal of Colloid Science **6** (4), 354-367 (1951).
144. F. Folgar and C. L. Tucker, J. Reinf. Plast. Compos. **3**, 98-119 (1984).
145. A. Vaccaro and G. Marrucci, Journal of Non-Newtonian Fluid Mechanics **92** (2-3), 261-273 (2000).
146. J. G. H. Cifre, T. Barenbrug, J. D. Schieber and B. van den Brule, Journal of Non-Newtonian Fluid Mechanics **113** (2-3), 73-96 (2003).
147. E. K. Hobbie and D. J. Fry, Physical Review Letters **97** (3) (2006).
148. A. W. K. Ma, F. Chinesta, M. R. Mackley and A. Ammar, Int. J. Mat. Form. **1** (2), 83-88 (2008).
149. C. Singh, T. Quested, C. B. Boothroyd, P. Thomas, I. A. Kinloch, A. I. Abou-Kandil and A. H. Windle, Journal of Physical Chemistry B **106** (42), 10915-10922 (2002).
150. S. P. Papkov, M. M. Iovleva, L. P. Milkova, Kalmykov.Vd, Volokhin.Av and Kudryavt.Gi, Vysokomolekulyarnye Soedineniya Seriya B **15** (10), 757-759 (1973).
151. S. P. Papkov, M. M. Iovleva, L. P. Milkova, R. V. Antipova, Goukhber.Ss, Kudryavt.Gi, Volokhin.Av and Kalmykov.Vd, Vysokomolekulyarnye Soedineniya Seriya B **15** (5), 357-360 (1973).
152. G. Natale, M. C. Heuzey, P. J. Carreau, G. Ausias and J. Férec, AIChE Journal, **60** (4), 1476-1487 (2014).
153. T. Chatterjee and R. Krishnamoorti, Soft Matter, **9** (40), 9515-9529 (2013).
154. T. Feng, D. A. Hoagland and T. P. Russell, Langmuir **30** (4), 1072-1079 (2014).
155. S. R. Vora, B. Bognet, H. S. Patanwala, F. Chinesta and A. W. K. Ma, Langmuir, **31** (16), 4663-4672 (2015).